Accepted Manuscript

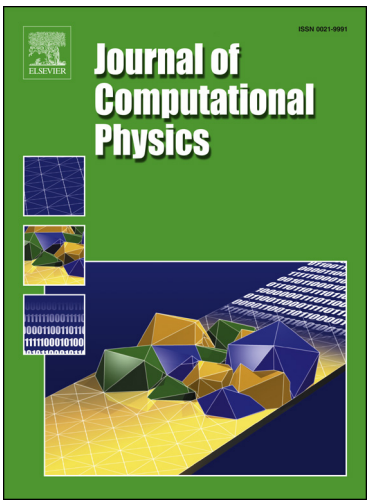

Mixing, scalar boundedness, and numerical dissipation in large-eddy simulations

Nek Sharan, Georgios Matheou, Paul E. Dimotakis

PII: S0021-9991(18)30297-3
DOI: https://doi.org/10.1016/j.jcp.2018.05.005
Reference: YJCPH 8004

To appear in: *Journal of Computational Physics*

Received date: 22 December 2017
Revised date: 17 April 2018
Accepted date: 4 May 2018

Please cite this article in press as: N. Sharan et al., Mixing, scalar boundedness, and numerical dissipation in large-eddy simulations, *J. Comput. Phys.* (2018), https://doi.org/10.1016/j.jcp.2018.05.005

Highlights

- Methods to enforce scalar boundedness in incompressible-flow simulations are proposed.
- Mixing metrics sensitive to the additional numerical dissipation are identified.
- Numerical-dissipation effects on mixing in large-eddy simulations are assessed.
- Performance of the proposed methods is examined for the first time by mixing metrics.

Mixing, scalar boundedness, and numerical dissipation in large-eddy simulations

Nek Sharan[a], Georgios Matheou[b], Paul E. Dimotakis[a]

[a] *Graduate Aerospace Laboratories, California Institute of Technology, Pasadena, CA 91125, USA*
[b] *Department of Mechanical Engineering, University of Connecticut, Storrs, CT 06269, USA*

Abstract

Numerical schemes for scalar transport and mixing in turbulent flows must be high-order accurate, and observe conservation and boundedness constraints. Discretization accuracy can be evaluated from the truncation error, and assessed by its dispersion and dissipation properties. Dispersion errors can cause violation of physical scalar bounds, whereas numerical dissipation is key to mitigating those violations. Numerical dissipation primarily alters the energy at small scales that are critical to turbulent mixing. Influence of additional dissipation on scalar mixing in large-eddy simulations (LES) of incompressible temporally evolving shear flow is examined in terms of the resolved passive-scalar field, $\tilde{Z}$. Scalar fields in flows with different mixing behavior, exhibiting both uniform and non-uniform mixed-fluid composition across a shear layer, are compared for different grid resolutions, subgrid-scale models, and scalar-convection schemes. Scalar mixing is assessed based on resolved passive scalar probability density function (PDF), variance, and spectra. The numerical-dissipation influence on mixing is found to depend on the nature of the flow. Mixing metrics sensitive to numerical dissipation are applied to examine the performance of limiting methods employed to mitigate unphysical scalar excursions. Two approaches, using a linear-scaling limiter for finite-volume schemes and a monotonicity-preserving limiter for finite-difference schemes, are studied. Their performance with respect to accuracy, conservation, and boundedness is discussed.

Keywords:
Scalar boundedness, Mixing, Numerical dissipation, Large-eddy simulations

1. Introduction

Passive or active scalar transport and mixing by turbulent flow is important in numerous engineering and scientific applications (e.g., [1, 2, 3] and references therein). Grid-resolution requirements and the resulting computational cost of simulations of high Reynolds- and Schmidt-number flows, where a wide range of spatial and temporal scales determine scalar mixing, place a direct calculation of all scales out of reach. Moreover, for high Schmidt numbers (Sc), the Batchelor scale ($\eta_\mathrm{B} \simeq \eta\, Sc^{-\frac{1}{2}}$) is smaller than the Kolmogorov scale (η), and a finer grid is required to fully resolve the scalar field than the velocity field. Large-eddy simulations (LES) lower the computational cost by modeling dynamic effects, on the resolved flow field, of spatial scales smaller than a cutoff wavenumber, while directly calculating the larger scales of motions [4, 5]. However, such modeling introduces subgrid-model errors in addition to numerical-discretization errors. Model errors are difficult to quantify without a corresponding direct numerical simulation (DNS) solution, which is usually out of reach for practical problems of engineering interest. Therefore, analyses of the interaction between the model and numerical errors are typically restricted to canonical flows at low to moderate Reynolds number [6, 7, 8, 9]. Several studies have examined the role of the filter-grid ratio $\Delta/\Delta x$ [8, 10, 11, 12], where Δ is the filter width and Δx is the grid spacing, and the discretization of the non-linear term [13, 14] in LES to

Email address: nsharan@caltech.edu (Nek Sharan)

keep numerical errors smaller than subgrid-scale (SGS) model contributions. These references and others (e.g. [15, 16]) study effects of LES model and numerical errors on the velocity field. In this work, effects of numerical-dissipation errors on a convected passive-scalar field, specifically on scalar boundedness and resolved and subgrid scalar-mixing estimates, are examined.

For uniform-density and uniform-diffusivity flow, the passive-scalar field, Z, is governed by the advection-diffusion equation

$$\frac{\partial Z}{\partial t} + u_j \frac{\partial Z}{\partial x_j} = \mathcal{D} \frac{\partial^2 Z}{\partial x_j^2}, \tag{1}$$

where u_j is the velocity and $\mathcal{D}$ denotes the diffusivity. Solutions to Eq. (1) obey the maximum principle, i.e., solution extrema can only occur at the (spatial or temporal) boundary, bounding Z by its initial and boundary values.

In practice, numerical solutions to Eq. (1) obtained from a high-order finite-difference/-volume method incur dispersion errors that may result in violations of the maximum principle. The high-wavenumber content of the solution is more susceptible to dispersion (phase-speed) errors, which are of concern to LES since such calculations are, by definition, under-resolved with higher energies at grid scale than if the flow were fully resolved.

If the SGS model does not provide adequate dissipation for a sufficiently smooth scalar field, dispersive oscillations can produce unphysical scalar excursions [17]. These excursions are commonly mitigated using upwind schemes [18, 19], or bound-preserving limiters [20, 21], both of which introduce artificial dissipation and can lower the accuracy of numerical solutions.

In this study, our aim is two-fold: (1) Examine the effect of numerical dissipation on mixed-fluid composition and scalar fluctuations in different mixing regimes of turbulent shear flows to identify flow statistics sensitive to additional dissipation. Mixed-fluid composition is assessed from scalar PDFs whereas scalar fluctuations from their second central moment, the variance. (2) Use flow statistics sensitive to additional dissipation to assess the numerical dissipation introduced by two limiting procedures, using the linear-scaling limiter of [22, 23] and the monotonicity-preserving limiter of [24], to enforce scalar boundedness.

From among the desirable properties of high-order accuracy, conservation, and boundedness, numerical schemes generally satisfy the former two properties but do not strictly impose the third. To enforce scalar boundedness, commonly-used approaches compromise either accuracy, for example with bound-preserving low-order schemes [18, 19, 21], or conservation, with semi-Lagrangian schemes employing bounded interpolation [20]. In this work, limiting approaches for incompressible-flow simulations that ensure scalar boundedness and conservation while preserving uniform high-order accuracy are discussed.

Liu & Osher [22] developed a linear-scaling limiter for scalar-conservation laws that was adapted to ensure boundedness with uniform high-order accuracy by Zhang & Shu [23] for finite-volume and discontinuous-Galerkin discretizations. The limiter was used in combination with a first-order scheme by Subbareddy *et al.* [21] to mitigate scalar excursions in compressible-flow simulations with finite-volume schemes. For incompressible-flow computations, a velocity reconstruction consistent with the incompressibility condition ensures boundedness without the need of incorporating a low-order scheme, thus ensuring uniform high-order accuracy. The reconstructions are shown for a velocity field calculated from the non-dissipative schemes of Morinishi *et al.* [25]. However, the limiting approach of [22, 23] cannot be applied to finite-difference schemes, which led us to explore the application of the monotonicity-preserving limiter of Suresh & Huynh [24] to enforce scalar boundedness with finite-difference schemes. Numerical dissipation introduced by each methodology is assessed based on scalar-mixing estimates in a canonical turbulent shear flow.

In Section 2.1, the LES governing equations and the SGS models used in this study are discussed. The evolution of scalar fields with initial conditions leading to different mixing behavior in the temporally-evolving shear flow is discussed in Section 2.2. Limiting approaches to mitigate unphysical scalar excursions in incompressible-flow simulations are discussed in Section 3. Several convection schemes with different dissipation and boundedness properties are examined and listed in Section 4.1 along with their global

scalar-excursion statistics. The effect of numerical-dissipation errors on scalar-mixing estimates is examined in Section 4.2. Scalar boundedness and numerical dissipation introduced by the limiting methodologies of Section 3 is assessed in Section 4.3.

2. Flow description

2.1. Governing equations and SGS models

For LES, the conservation equations are assumed to be spatially filtered using a kernel $G(\mathbf{x};\Delta)$, where Δ is the filter width, and a filtered (or resolved) quantity $\bar{f}(\mathbf{x},t)$ is obtained by convolution of $f(\mathbf{x},t)$ with $G(\mathbf{x};\Delta)$ [26]. An explicit convolution calculation is computationally expensive [11] and, in practice, the computational grid typically serves as the spatial filter, which with high-order schemes provides a cost-effective means for a desired accuracy [27]. The filtered conservation of mass, momentum, and passive-scalar equation for a uniform-density fluid are given by

$$\frac{\partial \bar{u}_j}{\partial x_j} = 0, \tag{2a}$$

$$\frac{\partial \bar{u}_i}{\partial t} + \frac{\partial \bar{u}_i \bar{u}_j}{\partial x_j} = -\frac{\partial p}{\partial x_i} + \nu \frac{\partial^2 \bar{u}_i}{\partial x_i^2} - \frac{\partial \tau_{ij}}{\partial x_j}, \tag{2b}$$

$$\frac{\partial \bar{Z}}{\partial t} + \frac{\partial \bar{u}_j \bar{Z}}{\partial x_j} = \frac{\nu}{Sc} \frac{\partial^2 \bar{Z}}{\partial x_j^2} - \frac{\partial q_j}{\partial x_j}, \tag{2c}$$

where ν is the kinematic viscosity and Sc denotes the Schmidt number with a scalar diffusivity $\mathcal{D} \equiv \nu/Sc$. The SGS stress tensor $\tau_{ij} = \overline{u_i u_j} - \bar{u}_i \bar{u}_j$ in the momentum equation and the SGS scalar flux $q_j = \overline{u_j Z} - \bar{u}_j \bar{Z}$ in the scalar-transport equation represent the dynamic effects of the subgrid scales of motion on the resolved flow field. They are closed in the present study using two SGS models, the stretched-vortex model and the dynamic-Smagorinsky model, to demonstrate that the results are generally independent of such a choice.

In the stretched-vortex model [28, 29], the SGS stress and scalar flux are given by

$$\tau_{ij} = \left(\delta_{ij} - e_i^\nu e_j^\nu\right) K, \tag{3}$$

$$q_j = -\frac{1}{2} \Delta K^{1/2} \left(\delta_{ij} - e_i^\nu e_j^\nu\right) \frac{\partial \bar{Z}}{\partial x_i}. \tag{4}$$

K is the subgrid kinetic energy, δ_{ij} is the Kronecker's delta, and e_i^ν is a unit vector aligned with the subgrid vortex. Readers are referred to [17] for further details on the implementation of the stretched-vortex model.

The choice of e_i^v as the most extensional unit eigenvector of the resolved strain-rate tensor, $\bar{S}_{ij} = \left(\partial \bar{u}_i/\partial x_j + \partial \bar{u}_j/\partial x_i\right)/2$, implies a positive SGS kinetic-energy dissipation rate, $\epsilon = -\tau_{ij}\bar{S}_{ij}$ [17]. The SGS scalar-variance dissipation rate, on the other hand,

$$\epsilon_{\text{sub}} = -q_j \frac{\partial \bar{Z}}{\partial x_j} \tag{5}$$

using (4) is positive for any choice of unit vector e_i^v since

$$\left(\frac{\partial \bar{Z}}{\partial x_i}\right)^2 \geq \left(e_i^v \frac{\partial \bar{Z}}{\partial x_i}\right)\left(e_j^v \frac{\partial \bar{Z}}{\partial x_j}\right).$$

The stretched-vortex model with e_i^v the most extensional unit eigenvector of $\bar{S}_{ij}$, therefore, prevents backscatter and the action of SGS terms of Eqs. (2b) and (2c) on the resolved velocity and scalar field, respectively, is purely diffusive. The filtered scalar value $\bar{Z}$ obtained from integrating (2c) is, therefore, bounded similarly as Z obtained from Eq. (1), for a divergence-free velocity field (2a).

The SGS scalar variance, $\sigma^2_{\rm sub}$, in the stretched-vortex model can be estimated from (e.g., [30, 31])

$$\sigma^2_{\rm sub} = 2\int_{\pi/\Delta}^{\infty} E^{\rm s}(k)\,{\rm d}k, \tag{6}$$

where $E^{\rm s}(k)$ denotes the scalar spectrum. For the evolution of a passive scalar mixed by a stretched-vortex velocity field, the scalar spectrum, derived in Pullin & Lundgren [32], is given by

$$E^{\rm s}(k) = K_{\rm s}\left\{k^{-5/3}\exp\left(-\frac{(4\nu+2\mathcal{D})k^2}{3\left|\bar{S}_v\right|}\right) + \frac{8}{5\pi}\left(\frac{\Gamma}{\pi\left|\bar{S}_v\right|}\right)^{1/3}k^{-1}\exp\left(-\frac{2\mathcal{D}k^2}{3\left|\bar{S}_v\right|}\right)\right\}, \tag{7}$$

where $\bar{S}_v \equiv -\left(\delta_{ij}-e^v_i e^v_j\right)\partial\bar{u}_i/\partial x_j$ is the magnitude of the strain rate aligned with the subgrid vortex axis and Γ denotes the subgrid vortex circulation that determines the relative magnitude of the k^{-1} Batchelor spectrum and $k^{-5/3}$ Obukov-Corrsin spectrum components in (7). $\Gamma = 1000\nu$ is recommended in [30, 31, 32] for the subgrid continuation of the scalar spectrum. The prefactor $K_{\rm s}$ is calculated from the local spherically-averaged second-order scalar structure function $\bar{F}^{\rm s}_2$,

$$K_{\rm s} = \frac{\bar{F}^{\rm s}_2}{A\Delta^{2/3} + B\left(\nu/\left|\bar{S}_v\right|\right)^{1/3}}, \qquad \bar{F}^{\rm s}_2 = \frac{1}{6}\sum_{j=1}^{3}\left(\left(\delta\bar{Z}^+\right)^2 + \left(\delta\bar{Z}^-\right)^2\right)_j, \tag{8}$$

where $B = 4\times(8/5\pi)\left(\Gamma/\pi\nu\right)^{1/3}\int_0^\pi s^{-1}\left(1-\sin s/s\right)\,{\rm d}s \approx 9.01726$.

Results from a dynamic eddy-viscosity SGS model [33] are also discussed. The SGS stress and scalar flux in an eddy-viscosity closure are given by

$$\tau_{ij} - \frac{1}{3}\delta_{ij}\tau_{kk} = -2\nu_{\rm T}\bar{S}_{ij} = -2C\Delta^2\left|\bar{S}\right|\bar{S}_{ij}, \tag{9}$$

$$q_j = -\frac{\nu_{\rm T}}{Sc_{\rm T}}\frac{\partial\bar{Z}}{\partial x_j}, \tag{10}$$

where $\left|\bar{S}\right| = \left(2\bar{S}_{ij}\bar{S}_{ij}\right)^{1/2}$. The coefficients C and $Sc_{\rm T}$ are determined from the Lagrangian averaging procedure of [34], which ensures that the coefficients are non-negative and there is no backscatter. The filtered scalar value $\bar{Z}$ obtained from integrating (2c) should, therefore, also be bounded by initial/boundary values for a divergence-free velocity field.

2.2. Initial conditions and flow characteristics

The same flow configuration is used as in [17], with a cubic domain of length $L = 4\pi\,{\rm m}$ and periodic boundary conditions in all three directions. Cartesian coordinates $(x,\,y,\,z)$ denote the streamwise, spanwise, and cross-stream directions, respectively, and $(u_1,\,u_2,\,u_3)\equiv(u,\,v,\,w)$ denote the corresponding velocity components. The kinematic viscosity, ν, is set to $1.7\times10^{-5}\,{\rm m}^2/{\rm s}$ with a Schmidt number of unity, i.e., $Sc \equiv \nu/\mathcal{D} = 1$, approximating gas-phase diffusion, are assumed in all simulations. The initial velocity components are given by

$$\bar{u}_i(x,y,z) = u'_i(x,y,z) - \frac{\partial p(x,y,z)}{\partial x_i}\Delta t, \tag{11}$$

where p is a Lagrange multiplier that imposes the divergence-free constraint, Δt denotes the time step, and

$$u'(x,y,z) = f(z) + a(z)\left[\sin 2k_0x + 0.01\cos 20y + r_1(x,y,z)\right], \tag{12a}$$

$$v'(x,y,z) = a(z)\left[\cos 2k_0x + 0.01\sin 20y + r_2(x,y,z)\right], \tag{12b}$$

$$w'(x,y,z) = a(z)\left[\sin k_0x + 0.01\cos 40y + r_3(x,y,z)\right]. \tag{12c}$$

The mean initial profile

$$f(z) = \tanh\left(40\ (\text{modulo}(z, 4\pi) - 2\pi)\right) - \tanh\left(40\ (\text{modulo}(z, 4\pi) - 4\pi)\right) - \tanh\left(40\,\text{modulo}(z, 4\pi)\right)$$

provides an alternating free-stream velocity of $u = \pm 1$ m/s and an initial momentum thickness of $\theta_0 = 0.0125$ m, calculated from

$$\theta = \int_{L/4}^{3L/4} \left[\frac{1}{4} - \left(\frac{\langle \bar{u} \rangle}{\Delta U}\right)^2\right] \mathrm{d}z,$$

where ΔU is the freestream velocity difference across the shear layer and angle brackets denote a horizontal average. The square brackets in (12a)–(12c) provide the initial perturbations to the velocity, confined to the initial mixing layer by

$$a(z) = 0.1 \exp[-100(\text{modulo}(z + \pi, 2\pi) - \pi)^2].$$

The r_i are random numbers in $[-0.5, 0.5]$. The initial condition for the passive scalar is

$$\bar{Z}(x, y, z) = (1 + f(z))/2, \tag{13}$$

which maps it to $Z \in [0, 1]$. No perturbations are added to the initial scalar field.

To study the effects of numerical dissipation on flows with different mixing characteristics, we choose an initial-velocity streamwise-perturbation wavenumber, k_0, in (12) that yields different flow regimes and mixed-fluid compositions across the shear layer. The role of initial disturbances in the evolution of mixing layers is discussed in [35, 36, 37, 38, 39], for example.

Mixed-fluid composition can be assessed from scalar PDFs. Figures 1 and 2 show scalar isosurfaces and PDFs at different times for $k_0 = 1$ and 2 m^{-1}, respectively. The entrainment of freestream fluid develops a near-uniform mixed-fluid composition within the shear layer in early stages, as shown in Figures 1(b) and 2(b), while the flow exhibits large-scale two-dimensional organization. It transitions to a non-uniform composition by $t = 20$ s for $k_0 = 2$ m^{-1}, as evident from Figure 2(c), while the scalar field for $k_0 = 1$ m^{-1} retains the near-uniform composition as late as $t = 20$ s.

Changes to mixed-fluid composition in time can be determined from the scalar variance about the global mixed-fluid mean concentration,

$$[\![\bar{Z}]\!] = \int_{\zeta}^{1-\zeta} \mathcal{Z}\, \mathcal{P}(\mathcal{Z})\ d\mathcal{Z}, \tag{14}$$

with a global scalar variance given by

$$\sigma^2_{\text{global}} = \int_{\zeta}^{1-\zeta} \left(\mathcal{Z} - [\![\bar{Z}]\!]\right)^2 \mathcal{P}(\mathcal{Z})\ d\mathcal{Z}, \tag{15}$$

where $\mathcal{P}(\mathcal{Z})$ is the resolved-scalar PDF of the mixed fluid. A value of $\zeta = 1/50$ is used as a threshold between mixed and unmixed fluid. A non-uniform composition with spatially varying most-probable scalar concentration will have higher deviations about the global mean, $[\![\bar{Z}]\!] \approx 1/2$, than a uniform composition. As a result, the scalar variance, σ^2_{global}, can exhibit a minimum, as shown in Figure 3 for the scalar field that develops from each initial perturbation considered. A minimum in variance indicates high mixedness.

The time scale $\tau = 1/(k_0 \Delta U)$ scales different flow stages, independent of the choice of k_0, as shown in Figure 3(b). The non-dimensional times of minimum variance are similar for shear flows with different initializations that produce mixing regimes with both a near-uniform and non-uniform mixed-fluid composition, as evident in Figures 1 and 2. This allows a study of the numerical-dissipation influence on mixing as well as the time of transition between the two mixing regimes. For analysis in Section 4, we consider only flows from $k_0 = 2$ m^{-1} or $k_0 L = 8\pi$. Other perturbation choices for k_0 yield similar results and conclusions.

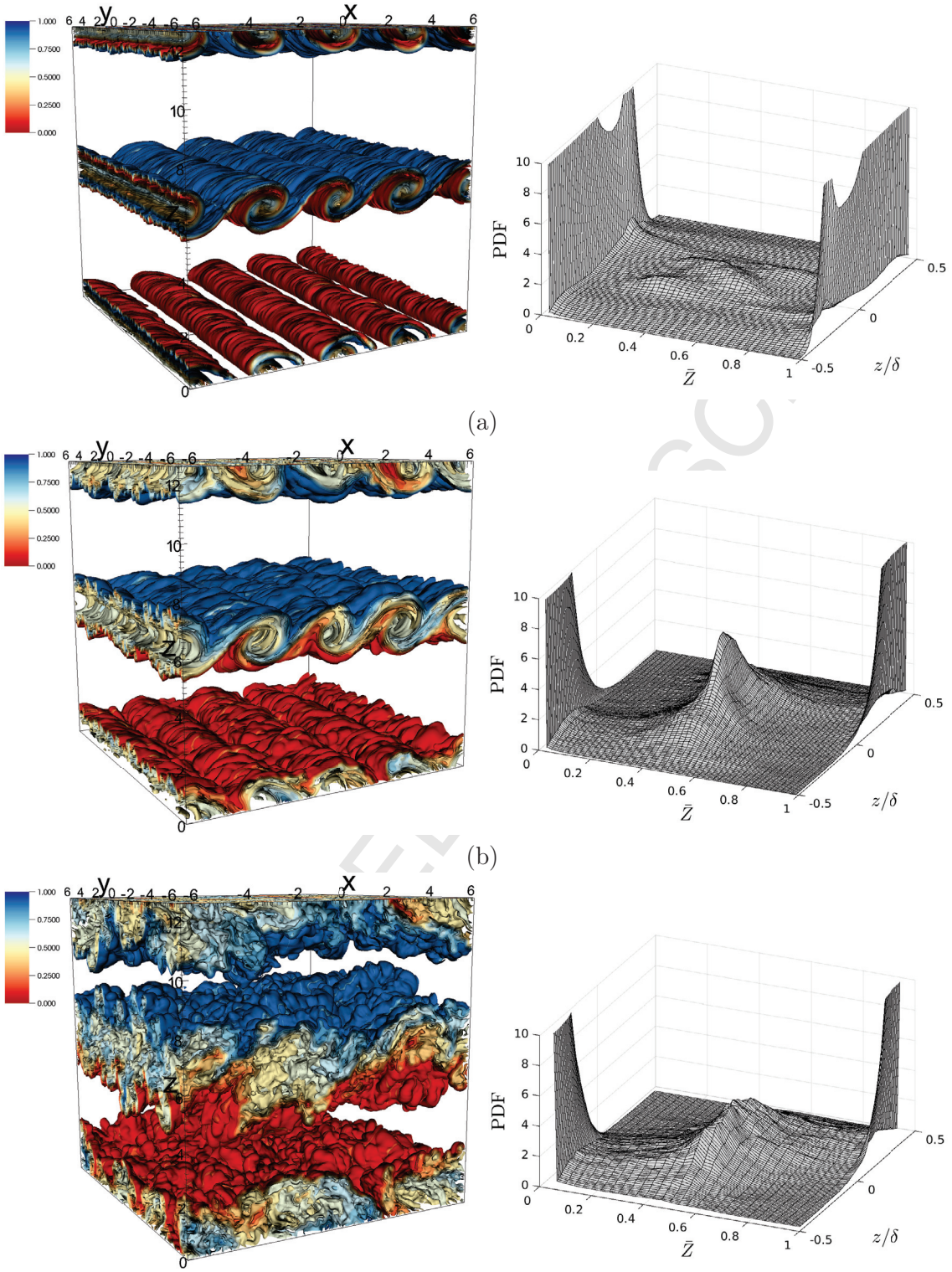

Figure 1: Scalar isosurfaces (left column) and resolved-scalar PDF (right column) at (a) $t = 5\,\mathrm{s}$ ($t/\tau = 10$), (b) $t = 10\,\mathrm{s}$ ($t/\tau = 20$) and (c) $t = 20\,\mathrm{s}$ ($t/\tau = 40$) from the initial condition with $k_0 = 1\,\mathrm{m}^{-1}$ ($k_0 L = 4\pi$) in Eq. (12).

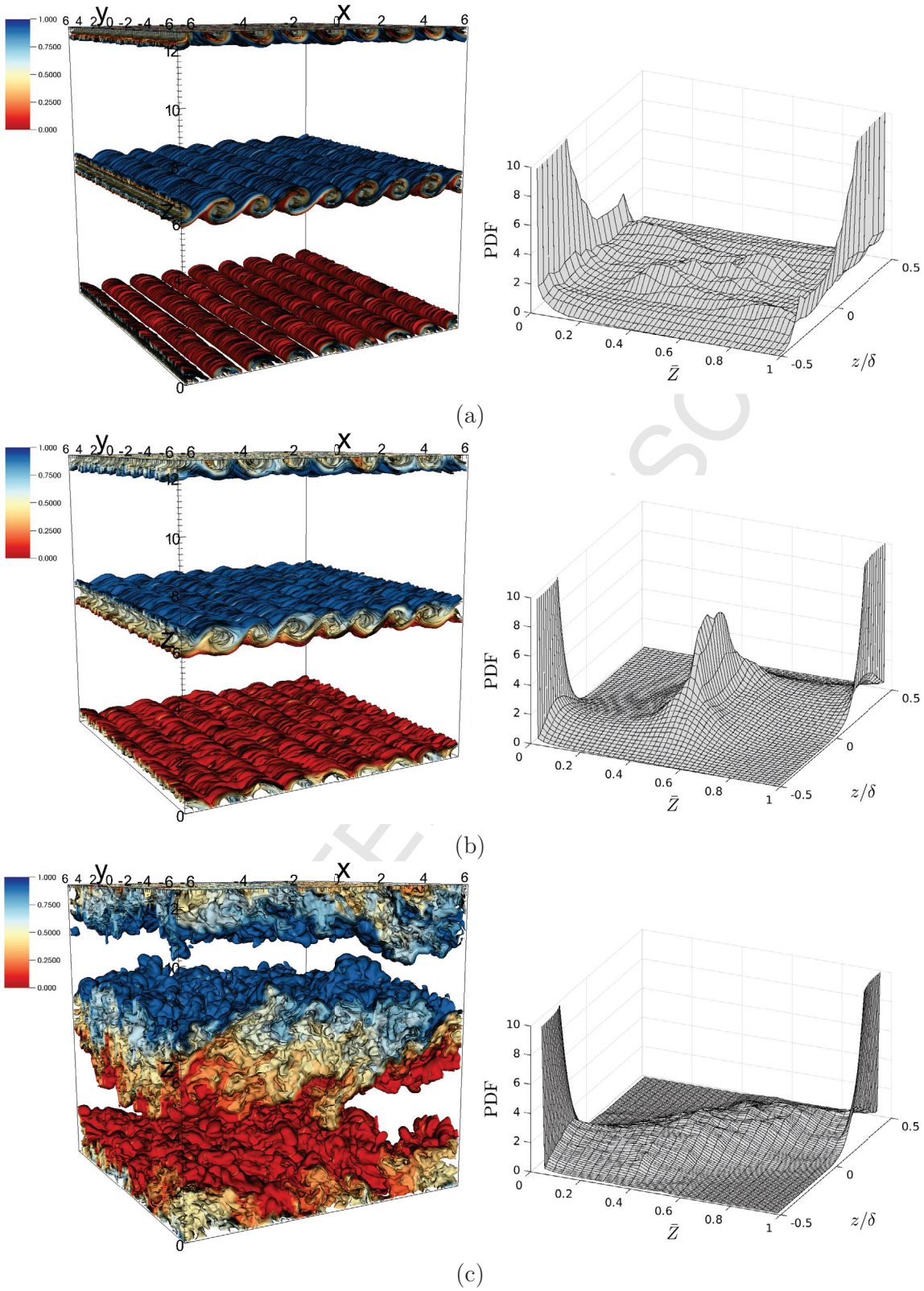

Figure 2: Scalar isosurfaces (left column) and resolved-scalar PDF (right column) at (a) $t = 3\,\mathrm{s}$ ($t/\tau = 12$), (b) $t = 5\,\mathrm{s}$ ($t/\tau = 20$) and (c) $t = 20\,\mathrm{s}$ ($t/\tau = 80$) from the initial condition with $k_0 = 2\,\mathrm{m}^{-1}$ ($k_0 L = 8\pi$) in Eq. (12).

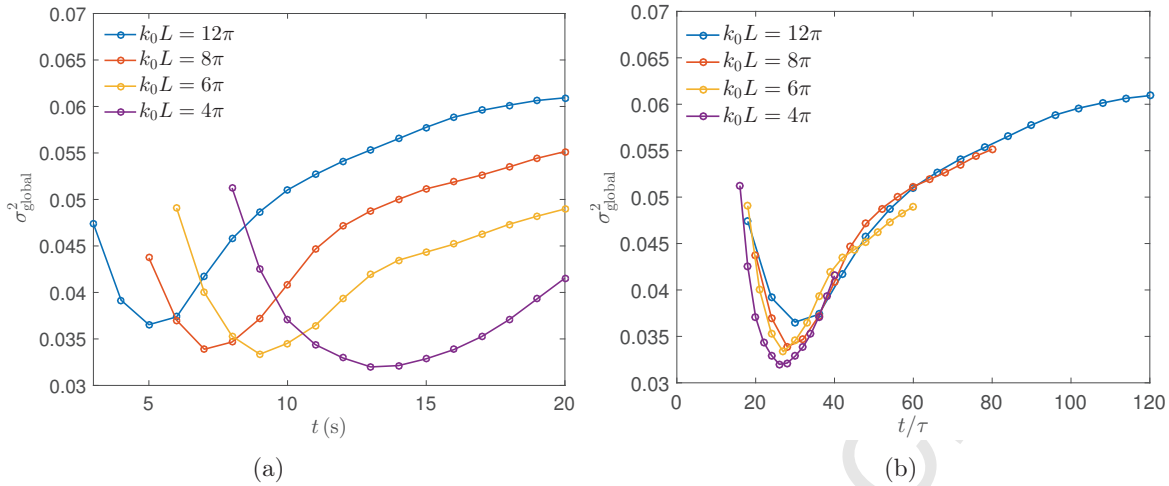

Figure 3: Resolved global scalar variance for different streamwise wavenumber of initial perturbation plotted against (a) dimensional, and (b) scaled time.

3. Methods to mitigate unphysical scalar excursions

In applications, especially involving active scalars, scalar transport must observe strict physical bounds. For example, the transport of absolute temperature or specific humidity in weather prediction must yield non-negative values, or values that do not exceed thermodynamic bounds, at all times. Similarly, species mass fractions in reacting flows or pollutant concentrations in environmental flows must be in the range $[0, 1]$ at all times.

Non-dissipative schemes tend to violate physical scalar bounds because of dispersive errors [17], whereas low-order upwind schemes can be effective in restricting such violations. Flux-limited [40] or flux-corrected-transport (FCT) [41] methods provide a framework to combine the two schemes, where the contribution from each is determined based on the smoothness of the solution by a limiter. An example of the flux-limited scheme that ensures monotonicity and thus boundedness, uses the Lax-Wendroff and the first-order upwind scheme with a total-variation diminishing (TVD) limiter [42, Chapter 16]. It is used in Section 4 to examine the numerical-dissipation influence on scalar boundedness and mixing estimates. Hybrid schemes of similar kind and of high-order accuracy have been extensively used for shock-dominated turbulent flows [43, 44, 45, 46], but these schemes are not TVD and do not strictly enforce boundedness or monotonicity.

A TVD scheme where the total variation is measured from grid values degenerates to first-order accuracy near smooth extrema [47], therefore for a derivation of non-oscillatory high-order schemes, the TVD condition is relaxed by a total-variation bounded (TVB) or a non-oscillatory condition [22, 48, 49]. In Sections 3.1 and 3.2, we discuss two limiting procedures based on the idea of non-oscillatory bounded and monotonic flux reconstructions, respectively, that ensure scalar boundedness without loss of accuracy. The first uses the maximum-principle-satisfying approach of Zhang & Shu [23] for finite-volume schemes and the second applies the monotonicity-preserving approach of Suresh & Huynh [24] to finite-difference schemes. The implementation and additional conditions for scalar boundedness on staggered grid are provided below.

To discuss limiting procedures, it is sufficient to consider the inviscid scalar equation,

$$\frac{\partial Z}{\partial t} + \frac{\partial f_k}{\partial x_k} = 0, \tag{16}$$

with the incompressibility condition $\partial u_k/\partial x_k = 0$ and a convective flux $f_k = u_k Z$. The viscous and SGS terms of Eq. (2c) can be ignored provided their numerical discretization retains the physically diffusive character that respects the maximum principle. The overbar denoting resolved quantities in (2c) is dropped in (16) to simplify notation, and reserved to denote cell averages in this section.

3.1. Bounded finite-volume scheme

For simplicity, consider a cell $\mathcal{C}_{ij}$ in a two-dimensional Cartesian grid, as shown in Figure 4. The extension to three-dimensions follows a similar approach. A staggered-grid arrangement, with scalar values stored at the cell center and velocity components at cell edges (faces in 3D), is used for all calculations. Integrating Eq. (16) over the cell $\mathcal{C}_{ij}$ and application of the divergence theorem yields an equation for cell averages. A finite-volume semi-discretization of the equation is given by

$$\frac{\mathrm{d}\bar{Z}_{ij}}{\mathrm{d}t} = -\frac{1}{\Delta x}\left(f_{i+\frac{1}{2},j} - f_{i-\frac{1}{2},j}\right) - \frac{1}{\Delta y}\left(g_{i,j+\frac{1}{2}} - g_{i,j-\frac{1}{2}}\right), \tag{17}$$

where $\bar{Z}_{ij}(t)$ is an approximation to the (i,j)-cell average of $Z(x,y,t)$,

$$\bar{Z}_{ij} \approx \frac{1}{\Delta x\,\Delta y}\int_{y_{j-\frac{1}{2}}}^{y_{j+\frac{1}{2}}}\int_{x_{i-\frac{1}{2}}}^{x_{i+\frac{1}{2}}} Z(x,y,t)\;dx\,dy, \tag{18}$$

and flux approximations, using $f_k = u_k Z$, are described by

$$f_{i+\frac{1}{2},j} \approx \frac{1}{\Delta y}\int_{y_{j-\frac{1}{2}}}^{y_{j+\frac{1}{2}}} f_1\left(Z(x_{i+\frac{1}{2}},y,t), u(x_{i+\frac{1}{2}},y,t)\right)\;dy, \tag{19}$$

$$g_{i,j+\frac{1}{2}} \approx \frac{1}{\Delta x}\int_{x_{i-\frac{1}{2}}}^{x_{i+\frac{1}{2}}} f_2\left(Z(x,y_{j+\frac{1}{2}},t), v(x,y_{j+\frac{1}{2}},t)\right)\;dx. \tag{20}$$

Following [23], assume a polynomial $p_{ij}(x,y)$ of degree k in x and y that approximates the scalar field in cell $\mathcal{C}_{ij}$ with cell average

$$\bar{Z}_{ij} = \frac{1}{\Delta x\,\Delta y}\int_{y_{j-\frac{1}{2}}}^{y_{j+\frac{1}{2}}}\int_{x_{i-\frac{1}{2}}}^{x_{i+\frac{1}{2}}} p_{ij}(x,y)\;dx\,dy = \sum_{a=1}^{n}\sum_{b=1}^{n} w_a w_b\, p_{ij}\left(\hat{x}_a,\hat{y}_b\right), \tag{21}$$

where $\hat{x}_a$ and $\hat{y}_b$ denote the quadrature points in the x- and y-direction, respectively, and w_a and w_b are the corresponding quadrature weights. In this study, the Gauss-Legendre quadrature is used, and hence the last equality in (21) assumes $2n-1 \geq k$, i.e., the quadrature rule in (21) is exact for polynomials of degree up to $2n-1$ in x and y. A multi-dimensional polynomial, $p_{ij}(x,y)$, that satisfies (21) is available for schemes that construct such a polynomial to advance the solution, such as the finite-volume WENO scheme of Dumbser *et al.* [50]. However, for schemes that perform a split dimension-by-dimension reconstruction, such as the finite-volume WENO scheme of Liu *et al.* [51], the polynomial needs to be constructed anew. In Sections 4.1 and 4.3, we discuss results from both WENO schemes, where a polynomial-reconstruction procedure similar to [23, Section 3.3] is used for the scheme of Liu *et al.* [51].

To enforce scalar boundedness, the polynomial is processed by the linear-scaling limiter of [22, 23],

$$\tilde{p}_{ij}(x,y) = \theta\left(p_{ij}(x,y) - \bar{Z}_{ij}\right) + \bar{Z}_{ij}, \qquad \theta = \min\left\{\frac{\left|M - \bar{Z}_{ij}\right|}{\left|M_{ij} - \bar{Z}_{ij}\right|}, \frac{\left|m - \bar{Z}_{ij}\right|}{\left|m_{ij} - \bar{Z}_{ij}\right|}, 1\right\}, \tag{22}$$

where $M_{ij} = \max\limits_{(x,y)\in S_{ij}} p_{ij}(x,y)$ and $m_{ij} = \min\limits_{(x,y)\in S_{ij}} p_{ij}(x,y)$. S_{ij} denotes the set of quadrature and cell-edge points given by

$$S_{ij} = S_i^x \otimes S_j^y, \qquad S_i^x = \left\{x_{i-\frac{1}{2}}, \hat{x}_1, \cdots, \hat{x}_n, x_{i+\frac{1}{2}}\right\}, \qquad S_j^y = \left\{y_{j-\frac{1}{2}}, \hat{y}_1, \cdots, \hat{y}_n, y_{j+\frac{1}{2}}\right\},$$

where $\otimes$ denotes a tensor product, which yields $S_i^x \otimes S_j^y = \left\{(x,y) : x \in S_i^x,\, y \in S_j^y\right\}$. M and m denote the physical upper and lower bound of scalar values. For the initial scalar field (13), $M = 1$ and $m = 0$.

The fluxes $f_{i+\frac{1}{2},j}$ and $g_{i,j+\frac{1}{2}}$, given by (19) and (20), are calculated from

$$f_{i+\frac{1}{2},j} = \sum_{b=1}^{n} w_b \hat{f}\left(Z^L_{i+\frac{1}{2},b}, Z^R_{i+\frac{1}{2},b}, u_{i+\frac{1}{2},b}\right), \qquad g_{i,j+\frac{1}{2}} = \sum_{a=1}^{n} w_a \hat{f}\left(Z^L_{a,j+\frac{1}{2}}, Z^R_{a,j+\frac{1}{2}}, v_{a,j+\frac{1}{2}}\right), \tag{23}$$

where $Z^L_{i+\frac{1}{2},b}$ and $Z^R_{i+\frac{1}{2},b}$ are approximations to $Z(x_{i+\frac{1}{2}}, \hat{y}_b, t)$ in cells $\mathcal{C}_{ij}$ and $\mathcal{C}_{i+1,j}$, respectively, and similarly $Z^L_{a,j+\frac{1}{2}}$ and $Z^R_{a,j+\frac{1}{2}}$ are approximations to $Z(\hat{x}_a, y_{j+\frac{1}{2}}, t)$ in cells $\mathcal{C}_{ij}$ and $\mathcal{C}_{i,j+1}$, respectively. They are obtained, using the limited polynomial (22), from

$$Z^L_{i+\frac{1}{2},b} = \tilde{p}_{ij}(x_{i+\frac{1}{2}}, \hat{y}_b), \qquad Z^R_{i+\frac{1}{2},b} = \tilde{p}_{i+1,j}(x_{i+\frac{1}{2}}, \hat{y}_b),$$

$$Z^L_{a,j+\frac{1}{2}} = \tilde{p}_{ij}(\hat{x}_a, y_{j+\frac{1}{2}}), \qquad Z^R_{i+\frac{1}{2},b} = \tilde{p}_{i,j+1}(\hat{x}_a, y_{j+\frac{1}{2}}).$$

To simplify implementation in an existing solver, the velocity field calculated from the momentum equations, stored at the cell edges, is used in (23). No reconstructions are performed for the velocity components. If the velocity components are not available at quadrature points, e.g., when finite-difference approximations are used for the spatial derivatives of momentum equations, as is the case for results shown in Section 4, $u_{i+\frac{1}{2},b} = u_{i+\frac{1}{2},j}$ and $v_{a,j+\frac{1}{2}} = v_{i,j+\frac{1}{2}}$ is assumed, which does not influence the accuracy of (23). We use the upwind flux for $\hat{f}$, given by

$$\hat{f}(Z^L, Z^R, u) = \frac{1}{2}\left[u\left(Z^R + Z^L\right) - |u|\left(Z^R - Z^L\right)\right]. \tag{24}$$

If the computed velocity field, u, and the constructed cell-interface scalar values, Z^L and Z^R, are of the same order of accuracy, then the flux $\hat{f}(Z^L, Z^R, u)$ preserves that accuracy.

For discretization (17) to ensure scalar boundedness with fluxes given by (23), a proof similar to [23, Theorem 4.3] shows that the computed velocity field must exactly satisfy

$$\frac{u_{i+\frac{1}{2},j} - u_{i-\frac{1}{2},j}}{\Delta x} + \frac{v_{i,j+\frac{1}{2}} - v_{i,j-\frac{1}{2}}}{\Delta y} = 0. \tag{25}$$

The incompressible-flow simulations discussed in this paper, calculate the divergence of the velocity in the pressure-Poisson equation on a staggered grid using the derivative approximations

$$\frac{\partial \phi}{\partial x} \approx \frac{\phi_{i+\frac{1}{2},j} - \phi_{i-\frac{1}{2},j}}{\Delta x}, \tag{26a}$$

$$\frac{\partial \phi}{\partial x} \approx \frac{9}{8}\left(\frac{\phi_{i+\frac{1}{2},j} - \phi_{i-\frac{1}{2},j}}{\Delta x}\right) - \frac{1}{8}\left(\frac{\phi_{i+\frac{3}{2},j} - \phi_{i-\frac{3}{2},j}}{3\Delta x}\right), \tag{26b}$$

$$\frac{\partial \phi}{\partial x} \approx \frac{150}{128}\left(\frac{\phi_{i+\frac{1}{2},j} - \phi_{i-\frac{1}{2},j}}{\Delta x}\right) - \frac{25}{128}\left(\frac{\phi_{i+\frac{3}{2},j} - \phi_{i-\frac{3}{2},j}}{3\Delta x}\right) + \frac{3}{128}\left(\frac{\phi_{i+\frac{5}{2},j} - \phi_{i-\frac{5}{2},j}}{5\Delta x}\right), \tag{26c}$$

for second-, fourth- and sixth-order accuracy, respectively. (26a) automatically satisfies (25) but for the fourth- and the sixth-order stencils, $u_{i+\frac{1}{2},j}$ in (17) must be reconstructed as, respectively,

$$u_{i+\frac{1}{2},j} = \frac{13}{12}u_{i+\frac{1}{2},j} - \frac{1}{12}\left(\frac{u_{i+\frac{3}{2},j} + u_{i-\frac{1}{2},j}}{2}\right),$$

$$u_{i+\frac{1}{2},j} = \frac{1067}{960}u_{i+\frac{1}{2},j} - \frac{29}{240}\left(\frac{u_{i+\frac{3}{2},j} + u_{i-\frac{1}{2},j}}{2}\right) + \frac{3}{320}\left(\frac{u_{i+\frac{5}{2},j} + u_{i-\frac{3}{2},j}}{2}\right),$$

with a similar reconstruction for $v_{i,j+\frac{1}{2}}$ to ensure that (25) holds exactly and that scalar boundedness is enforced with uniform high-order accuracy.

The CFL condition for scalar boundedness in the two-dimensional case discussed above is given by (see [23])

$$\max\left(|u|\frac{\Delta t}{\Delta x} + |v|\frac{\Delta t}{\Delta y}\right) \leq \min_{a=1,\cdots n} w_a.$$

For $n = 3$ and 4, where n is the number of quadrature points, the Gauss-Legendre quadrature yields a CFL number of 0.28 and 0.17, respectively. In practice, a CFL number up to 0.3 provides bounded results for multiple test problems that were examined with both values of n. Numerical results discussed in Section 4.3 use $n = 3$ for the WENO scheme of Liu *et al.* [51] and $n = 4$ for the WENO scheme of Dumbser *et al.* [50] with a CFL number of 0.3 for both.

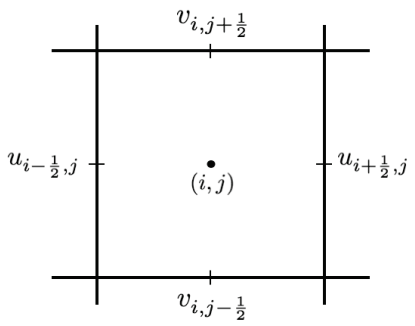

Figure 4: Cell $\mathcal{C}_{ij} = [x_{j-\frac{1}{2}}, x_{j+\frac{1}{2}}] \times [y_{j-\frac{1}{2}}, y_{j+\frac{1}{2}}]$ in a two-dimensional staggered-grid configuration. Scalar values are stored at the cell center and velocity components at the cell edges (faces in 3D).

3.2. Bounded finite-difference scheme

In Suresh & Huynh [24], monotonicity-preserving bounds are derived for cell-interface values of a finite-difference discretization of Eq. (16) to enforce monotonicity, and thus scalar boundedness. Consider a semi-discretization for a two-dimensional flow, on a staggered-grid configuration as shown in Figure 4,

$$\frac{\mathrm{d}Z_{ij}}{\mathrm{d}t} = -\frac{1}{\Delta x}\left(u_{i+\frac{1}{2},j}Z_{i+\frac{1}{2},j} - u_{i-\frac{1}{2},j}Z_{i-\frac{1}{2},j}\right) - \frac{1}{\Delta y}\left(v_{i,j+\frac{1}{2}}Z_{i,j+\frac{1}{2}} - v_{i,j-\frac{1}{2}}Z_{i,j-\frac{1}{2}}\right), \tag{27}$$

where the cell-interface scalar values, $Z_{i+\frac{1}{2},j}$ and $Z_{i,j+\frac{1}{2}}$, are computed from any high-order accurate construction, e.g., the centered construction of Morinishi *et al.* [25], the WENO construction of Jiang & Shu [52], etc. These constructions lead to violations of physical scalar bounds, as discussed in Section 4.1. In [24], Suresh & Huynh propose a limiter for reconstruction of cell-interface values to preserve monotonicity, without loss of accuracy, if the solution is monotonic at the current time, where monotonicity is measured on a stencil width. The (monotonicity-preserving) limiter is given by

$$Z_{i+\frac{1}{2},j} = \text{median}\,(Z_{i+\frac{1}{2},j}, Z^{\min}_{i+\frac{1}{2},j}, Z^{\max}_{i+\frac{1}{2},j}), \tag{28}$$

where $Z_{i+\frac{1}{2},j}$ on the LHS is the reconstructed value, whereas that on the RHS is from any construction (that may violate monotonicity). $Z^{\min}_{i+\frac{1}{2},j}$ and $Z^{\max}_{i+\frac{1}{2},j}$ are obtained from

$$Z^{\min}_{i+\frac{1}{2},j} = \max\left[\min\left(Z_{ij}, Z_{i+1,j}, Z^{\mathrm{MD}}_{i+\frac{1}{2},j}\right), \min\left(Z_{ij}, Z^{\mathrm{UL}}_{i+\frac{1}{2},j}, Z^{\mathrm{LC}}_{i+\frac{1}{2},j}\right)\right],$$

$$Z^{\max}_{i+\frac{1}{2},j} = \min\left[\max\left(Z_{ij}, Z_{i+1,j}, Z^{\mathrm{MD}}_{i+\frac{1}{2},j}\right), \max\left(Z_{ij}, Z^{\mathrm{UL}}_{i+\frac{1}{2},j}, Z^{\mathrm{LC}}_{i+\frac{1}{2},j}\right)\right],$$

where the upper-limit (UL), median (MD) and large-curvature (LC) allowance are given by

$$Z^{\mathrm{UL}}_{i+\frac{1}{2},j} = Z_{ij} + \alpha\,(Z_{ij} - Z_{i-1,j})\,, \tag{29a}$$

$$Z^{\mathrm{MD}}_{i+\frac{1}{2},j} = \frac{1}{2}(Z_{ij} + Z_{i+1,j}) - \frac{1}{2}d^{M4}_{i+\frac{1}{2},j}, \tag{29b}$$

$$Z^{\mathrm{LC}}_{i+\frac{1}{2},j} = Z_{ij} + \frac{1}{2}(Z_{ij} - Z_{i-1,j}) + \frac{4}{3}d^{M4}_{i-\frac{1}{2},j}. \tag{29c}$$

$d^{M4}_{i+\frac{1}{2},j}$ denotes a measure of the curvature defined as

$$d^{M4}_{i+\frac{1}{2},j} = \text{minmod}(4d_{ij} - d_{i+1,j}, 4d_{i+1,j} - d_{ij}, d_{ij}, d_{i+1,j}),$$

$$d_{ij} = Z_{i+1,j} - 2Z_{ij} + Z_{i-1,j}.$$

The parameter α in (29a) determines the CFL number, which must be less than $1/(1+\alpha)$ for boundedness. We use $\alpha = 2$, i.e., a CFL number of 0.33, for the results discussed in Section 4.3. Eq. (28) provides the reconstruction for $Z_{i+\frac{1}{2},j}$. A similar reconstruction is performed in the $j-$direction for $Z_{i,j+\frac{1}{2}}$, following a dimension-by-dimension approach. Extension to three dimensions follows a similar approach.

The initial scalar field given by Eq. (13) is monotonic and, therefore, preserves monotonicity in the vicinity of global bounds, i.e., for $0 \leq \bar{Z} \leq \zeta$ and $1 - \zeta \leq \bar{Z} \leq 1$, eliminates unphysical scalar excursions. In Section 4.3, we use $\zeta = 0.05$. The limiter (28) can be applied to cell-interface values constructed from any finite-difference scheme, which provides great flexibility in the choice of numerical discretization. Moreover, the approach dynamically checks for monotonicity violations, and does not require a correction step as used in [18].

4. Numerical results

The turbulent shear flow described in Section 2.2 provides a suitable test problem to examine the performance of limiting methods discussed in the previous section. The flow is simple enough to enable a comparative analysis between different numerical schemes. At the same time, it captures regions and mixing regimes encountered in more complicated flows. Moreover, the choice of different initial perturbations generates flows with both near-uniform and non-uniform mixed-fluid composition, which allows an assessment of the effect of numerical-dissipation errors in different mixing regimes. For the results and analyses in this section, an initial perturbation of $k_0 L = 8\pi$ in (12) is used. Results from other perturbation choices were similar.

The LES equations (2) are solved on an Arakawa C (staggered) grid [53] with N grid points in each direction. The modified pressure, p', in (2b) is obtained by solving the pressure-Poisson equation, using discrete Fourier transforms, to satisfy the incompressibility divergence-free condition [54]. Time-integration is performed using the third-order TVD Runge-Kutta method of Shu & Osher [48]. The LES code with the stretched-vortex model was successfully used in [55, 56, 57] and similar dynamic-Smagorinsky model implementations were used in [58, 59, 60], where they have been tested and validated.

4.1. Unphysical scalar excursions and scalar spectra

The limiting approach described in Sections 3.1 and 3.2 can be applied to any finite-volume and finite-difference scheme, respectively, to enforce scalar boundedness. As a result, the dissipation error of limited methods will at best be similar to those of the underlying scheme. Therefore, before evaluating the performance of limiters, we examine the dispersion and dissipation properties of some of the commonly used numerical schemes for turbulent flow computation of the scalar field.

For smooth flows, the fully-conservative centered schemes [25] are preferred because of their non-dissipative character and low aliasing errors [61, 62]. For flows with strong gradients, centered schemes can cause significant dispersion errors. Therefore, upwind methods, such as QUICK [63], or non-oscillatory methods, such as weighted essentially non-oscillatory (WENO) schemes [51, 52], or hybrid approaches [43, 44, 45] are preferred. Table 1 shows the numerical schemes, and corresponding references, considered here for analysis.

WENO4 denotes the $r = 3$ (4th-order) finite-volume scheme of Liu *et al.* [51]. WENO5 is the $r = 3$ (5th-order) finite-difference scheme of Jiang & Shu [52]. WENO(D) denotes the $M = 4$ (5th-order) finite-volume scheme of Dumbser *et al.* [50], which differs from Liu *et al.* [51] by using Legendre polynomials as the reconstruction basis. TVD denotes a flux-limited scheme using the Lax-Wendroff and the first-order upwind scheme with a TVD limiter [42, 64].

To analyze unphysical scalar excursions that arise from errors in discretization of the scalar-convection term [17], only the discretization of the scalar-convection term is changed. In all cases, the fully-conservative fourth-order scheme of Morinishi *et al.* [25] is used to discretize the momentum-convection term. The corresponding fourth-order accurate approximation of the pressure-Poisson equation is solved by utilizing a Fourier expansion of the difference equation, similar to [54], resulting in a direct solution of the linear system of equations. The resolved viscous and SGS-model terms are discretized using the second-order centered approximations. The stretched-vortex SGS model is used with a filter width of the grid size, i.e., $\Delta = \Delta x$.

Symbol	Scalar-convection scheme
4th	4^{th}-order fully conservative (Morinishi *et al.* [25])
QUICK	QUICK (Leonard [63])
WENO(D)	5^{th}-order Legendre polynomial WENO (Dumbser *et al.* [50])
WENO5	5^{th}-order flux-based WENO (Jiang & Shu [52])
WENO4	4^{th}-order cell-averaged WENO (Liu *et al.* [51])
TVD	TVD flux-limited (Van Leer [64])

Table 1: Summary of scalar-convection schemes used for comparative study. Symbol denotes the label used in figures and tables.

Table 2 and Figure 5 summarize the global scalar-excursion statistics, i.e., overshoots and undershoots, from the schemes listed in Table 1 for the shear-flow LES using the stretched-vortex SGS model. Table 2 shows the volume fractions (scaled by the factors in the Multiplier column) of threshold violation given in Column 1. For example, 2.009×10^{-2} is the volume fraction of scalar values $\bar{Z} > 1.01$ at $t/\tau = 80$ when the fully-conservative fourth-order scheme (4th) is used for the discretization of the scalar-convection term. First five rows show overshoots and bottom five undershoots. The numerical schemes are arranged, from left to right, in descending order of degree of threshold violation from them. Figure 5 shows the maximum and minimum scalar value from different schemes with time.

Statistics from the dynamic-Smagorinsky SGS model, omitted for brevity, show a similar trend for different schemes but exhibit higher overshoots/undershoots in each case. The higher unphysical excursions could be attributed to lower diffusion from the dynamic-Smagorinsky SGS model, as also evident in the scalar-variance minima comparison in Figures 8(a) and (b).

WENO schemes ensure essentially non-oscillatory solutions by assigning more weight to the smoothest stencil among a choice of upwind, centered, and downwind stencils. However, this approach tends to excessively diffuse important flow features in turbulent flow simulations with smooth flow fields, such as the mixing layer discussed here. A straightforward step to reduce the amount of artificial diffusion, in such cases, is to substitute the smoothness-based stencil weights by the optimal weights. In Appendix B, we provide results from the use of optimal weights for each WENO scheme discussed above, denoting them by a suffix "-opt". The optimal WENO schemes are better suited for the mixing-layer simulation discussed here and are used in Section 4.3 to assess dissipation introduced by the limiting methods of Section 3.

The extent of scalar overshoots and undershoots from these methods provides a measure of the corresponding dispersion error, which can be assessed by a modified-wavenumber or phase-speed plot. Linear schemes, such as the fully-conservative schemes of Morinishi *et al.* [25], allow Fourier analysis to determine an explicit expression for modified wavenumber [65]. But such an approach cannot be applied to WENO and flux-limited schemes because of their nonlinearity owing to the solution-dependent stencil weights and the limiter, respectively. An approximate dispersion relation that accounts for the leading-order non-linear effect in these schemes is discussed in [66]. The scalar-excursion statistics provide a qualitative representation of dispersion errors regardless of the linearity of the numerical scheme. Among the schemes of different order-of-accuracy from Morinishi *et al.* [25], dispersion errors from the second-order method are largest, and so are the corresponding scalar overshoots and undershoots [17]. The solutions from WENO schemes show

overshoots of the same order as the QUICK scheme, but relatively small undershoots. This asymmetry is a result of the oscillatory velocity field, calculated using the fourth-order scheme of Morinishi *et al.* [25] in all cases, and the essentially non-oscillatory reconstruction of the scalar field that constitutes the convective flux, $f_j = \bar{u}_j\bar{Z}$, such that for $\bar{Z} \approx 1$, the flux $f_j = \bar{u}_j\bar{Z} \approx \bar{u}_j$ is oscillatory, whereas for $\bar{Z} \approx 0$, the flux $f_j \approx 0$ is essentially non-oscillatory. Therefore, unphysical excursions near $\bar{Z} = 0$, i.e., undershoots, are small. This is further confirmed by the observation that if an initial scalar value range of $\bar{Z} \in [-1, 1]$ is used in place of $\bar{Z} \in [0, 1]$, unphysical excursions are symmetric, i.e., overshoots and undershoots are of comparable magnitude. Appendix A discusses the implementation of WENO schemes, used in this study, on a staggered-grid configuration.

Scalar value	Volume fraction						
	Multiplier	Scalar-convection scheme					
		4th	QUICK	WENO(D)	WENO5	WENO4	TVD
> 1.01	10^{-2}	2.009	0.803	0.738	0.299	0.192	0
> 1.02	10^{-2}	1.074	0.386	0.180	0.038	0.024	0
> 1.05	10^{-3}	2.308	0.344	0.035	0.003	0.003	0
> 1.1	10^{-4}	2.709	0.012	0.0006	0	0	0
> 1.2	10^{-6}	5.782	0	0	0	0	0
$<$ -0.01	10^{-2}	2.147	0.781	0.0001	0	0	0
$<$ -0.02	10^{-2}	1.182	0.373	0	0	0	0
$<$ -0.05	10^{-3}	2.583	0.227	0	0	0	0
$<$ -0.1	10^{-4}	2.629	0	0	0	0	0
$<$ -0.2	10^{-6}	2.921	0	0	0	0	0

Table 2: Global scalar-excursion statistics at $t/\tau = 80$ from different numerical schemes applied to the scalar-convection term using $N = 256$ and the stretched-vortex SGS model.

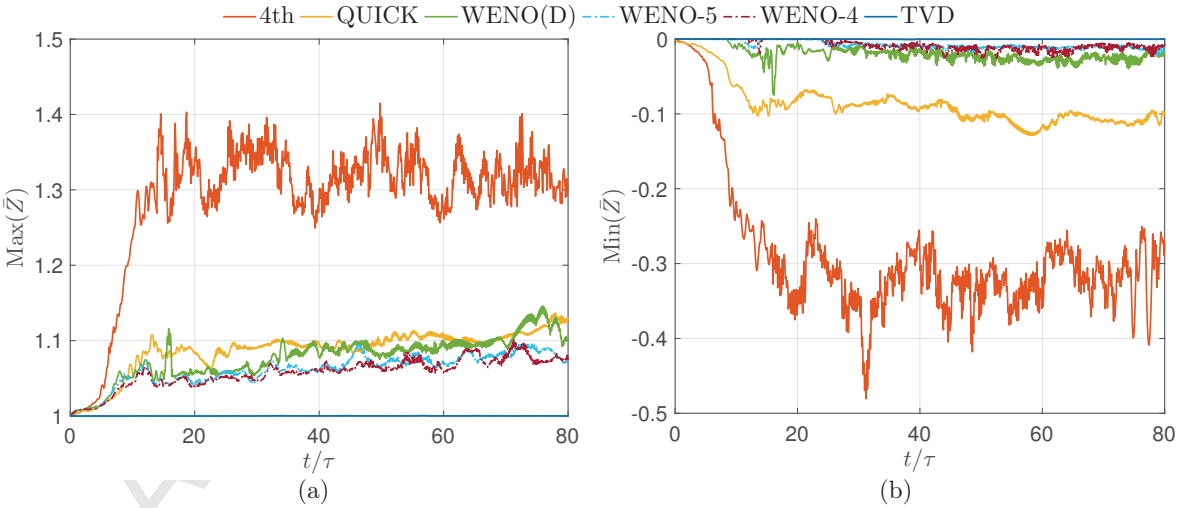

Figure 5: Global scalar excursion in simulations using different numerical schemes and $N = 256$ with the stretched-vortex SGS model. (a) Maximum overshoot, (b) Maximum undershoot.

The dissipation error of the schemes can be assessed from scalar spectra. Figure 6 shows one-dimensional resolved scalar and scalar-gradient spectra along the streamwise direction on the mixing layer mid-plane at $t/\tau = 80$ from different schemes, indicating a span of almost two decades with close to $k^{-5/3}$ scaling for this flow with $Re_\delta \simeq 5\times10^5$, as shown in the next section. The difference in area under the scalar spectra between any two schemes measures the scalar variance lost to numerical dissipation from the more dissipative scheme.

As discussed in [17], the fully-conservative centered schemes of Morinishi *et al.* [25] are least dissipative, whereas the flux-limited TVD scheme is most dissipative. QUICK and WENO schemes, interestingly, do not follow the same order in Figure 6 as Figure 5. The QUICK scheme causes relatively higher scalar excursions than the WENO schemes and, at the same time, is more dissipative than the WENO(D) scheme and equally as dissipative as the WENO4 and WENO5 schemes. It suggests that the dispersion and dissipation errors from the WENO schemes are smaller than the QUICK scheme.

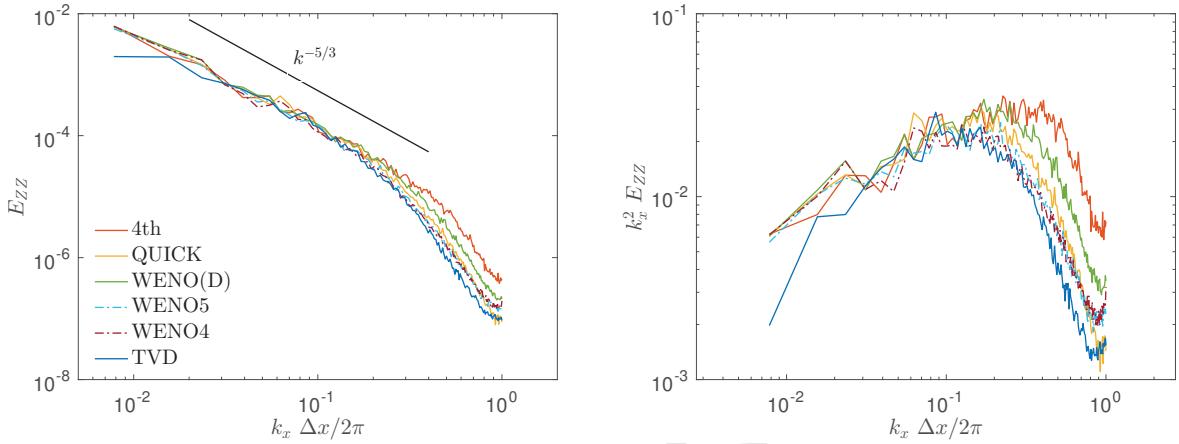

Figure 6: One-dimensional spectra along the streamwise direction on the mid-plane of mixing layer at $t/\tau = 80$ using $N = 256$ and the stretched-vortex SGS model. (a) Scalar spectra, E_{ZZ}, (b) scalar-gradient spectra $k_x^2 E_{zz}$.

4.2. Scalar mixing and numerical-dissipation effects

Turbulent mixing in LES occurs mostly at subgrid scales, which are sensitive to numerical dissipation that may be incurred in mitigation of unphysical scalar excursions. The effects of numerical dissipation on passive-scalar mixing and consistency of LES mixing statistics with respect to grid refinement are examined in this section. From the numerical schemes discussed in Section 4.1, we consider the fourth-order non-dissipative scheme of Morinishi *et al.* [25] and the flux-limited TVD scheme [64] that show contrasting behavior with respect to unphysical scalar excursions. The former produces significant scalar excursions because of dispersion errors. The latter suppresses all excursions because of its TVD character, but is very dissipative and reduces to first-order accuracy near local extrema. The grid-resolution influence is examined by performing simulations with $N = 256$ and 512, with coarse-grid simulations initialized by spectrally filtering and interpolating the solution of fine-grid simulation at $t/\tau = 32$ to facilitate comparisons.

4.2.1. Shear-layer width

The shear-layer width based on scalar concentration, denoted δ_Z, is defined here as the 1% scalar mean profile thickness, i.e., $0.01 \leq \langle \bar{Z} \rangle \leq 0.99$, where $\langle \bullet \rangle$ denotes a horizontal average. Similarly, the width based on streamwise velocity, denoted δ_u, is defined as the mean streamwise velocity profile thickness corresponding to $-0.49 \leq \langle \bar{u} \rangle / \Delta U \leq 0.49$. Figure 7 compares the growth of shear-layer width and the corresponding Reynolds number, Re_δ, with time between the fourth-order non-dissipative and the flux-limited TVD scheme with $N = 256$ and 512. The velocity field in each case is calculated using the fourth-order non-dissipative scheme and is not influenced by the passive-scalar field. Figure 7(a) shows the results from the stretched-vortex SGS model and Figure 7(b) from the dynamic-Smagorinsky model. The growth of the shear-layer width is seen to be nearly insensitive to numerical dissipation as well as to grid resolution, for both SGS models. By $t/\tau = 80$, the flow attains a Reynolds number, Re_δ, in excess of 5×10^5. To further understand the role of numerical dissipation, scalar-mixing estimates are examined in the next section.

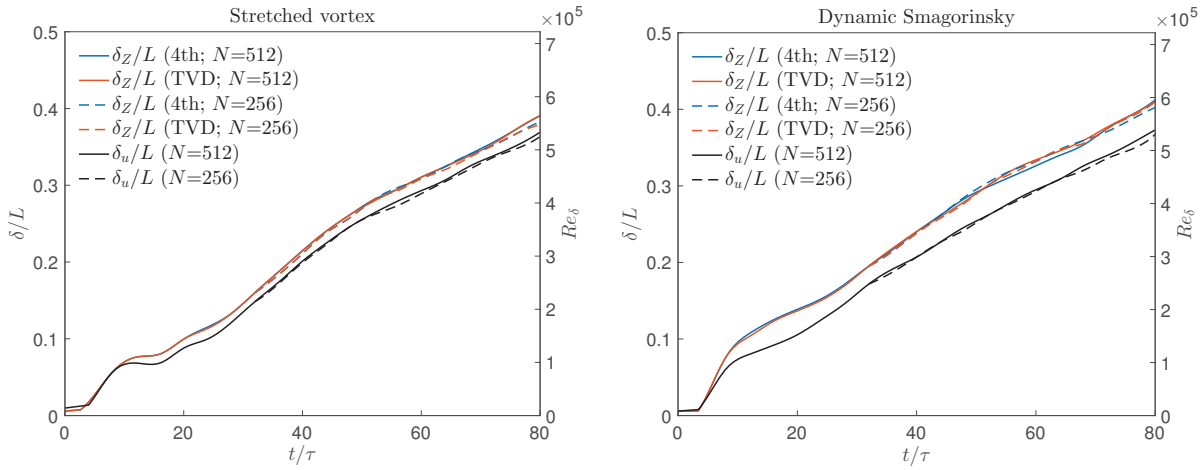

Figure 7: Evolution of shear-layer width and Re_δ from LES using different numerical schemes, grid resolutions, and (a) the stretched-vortex model, (b) the dynamic-Smagorinsky model.

4.2.2. Resolved scalar PDF and variance

Figure 3 represents the time evolution of the resolved variance of mixed-fluid composition in the shear flow investigated. It can be used to examine effects of numerical dissipation on scalar mixing at different stages of the shear-flow development. Figures 8(a) and (b) show the resolved scalar variance from fourth-order non-dissipative and TVD scheme at two grid resolutions, using the stretched-vortex and the dynamic Smagorinsky SGS model, respectively. As discussed in Section 2.2, the time of minimum variance ($t/\tau \approx 25$) corresponds to a state of (local) maximum mixedness, characterized by a near-uniform mixed-fluid composition. At times before the minimum variance, $t/\tau \lesssim 25$, scalar mixing generates a mixed-fluid concentration close to the global mean of 1/2 across the shear layer width, as shown in Figures 1(b) and 2(b), therefore, from Eq. (15) with $[\![\bar{Z}]\!] \approx 1/2$, scalar variance decreases locally with time. After the minimum variance, for $t/\tau \gtrsim 25$, the evolution to a less-uniform mixed-fluid composition leads to an increase in variance.

The TVD scheme artificially enhances mixing at all times compared to the non-dissipative scheme. The numerical-dissipation influence, as shown in Figures 8(a) and (b), is more pronounced at early times, before the scalar-variance minimum. Higher mixing at early times, $t/\tau < 25$, generates mixed-fluid with scalar concentration clustered around 1/2, which leads to a lower scalar variance from the TVD scheme with both SGS models. After the scalar-variance minimum, as the shear-layer width grows with time and the mixed-fluid composition becomes non-uniform, higher mixing generates a concentration close to 1/2 around the mid-plane and intermediate concentrations farther from 1/2 near the shear-layer edges. Concentrations close to 1/2 lower the global scalar variance whereas those farther from 1/2 increase it. At late times, the global scalar variance, therefore, is determined by the extent of mixing at the mid-plane versus that at the shear-layer edges. The stretched-vortex SGS model tends to homogenize the fluid at the mid-plane faster than the dynamic-Smagorinsky model and, therefore, the scalar-variance minimum is lower and the scalar variance from TVD scheme is higher at late times in Figure 8(a). Coarse-grid simulations, initialized at $t/\tau = 32$, predict higher resolved global variance with both SGS models.

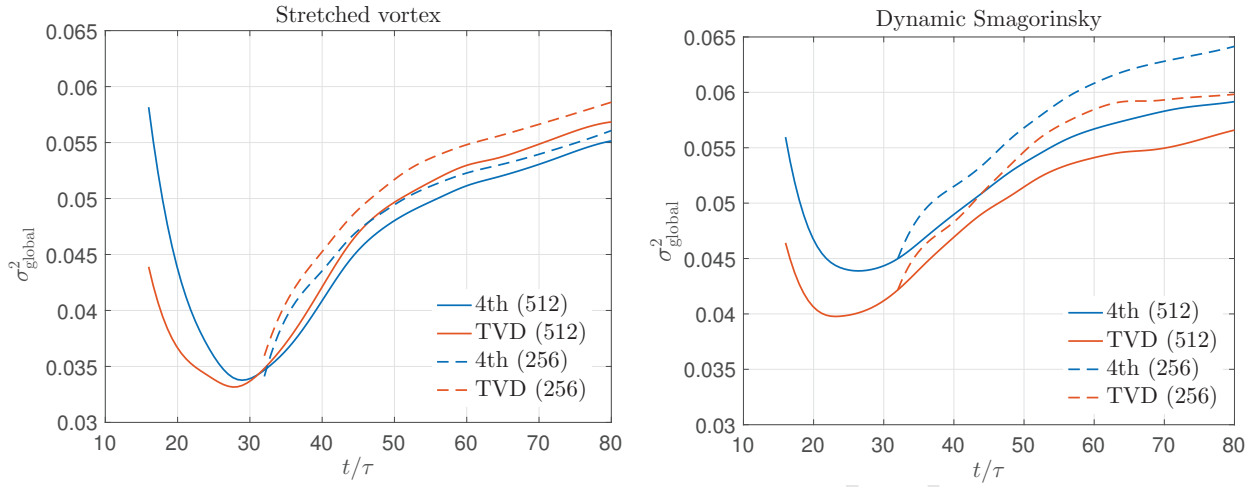

Figure 8: Resolved scalar variance comparison between the non-dissipative fourth-order and the TVD scheme using (a) the stretched-vortex SGS model, (b) the dynamic-Smagorinsky SGS model. Parentheses in legend label the number of grid points in each direction, N.

Mean and scalar variance calculated from (14) and (15), respectively, take the mixed fluid across the shear-layer width into account. As a result, the mean remains nearly constant, i.e., $[\![\bar{Z}]\!] \approx 1/2$ at all times, and Figure 8 shows the deviation of the mixed-fluid concentration about this (global) mean. An alternative estimate of scalar variance, σ^2_{local}, can be obtained by replacing $[\![\bar{Z}]\!]$ in (15) by the local or spatially-varying mean, $\langle \bar{Z} \rangle$, shown in Figure 9 for the scalar field at $t/\tau = 80$. σ^2_{local} represents local scalar fluctuations or physical stirring/mixing of fluid elements. Figure 10 shows σ^2_{local} at a time before ($t/\tau = 16$) and after ($t/\tau = 80$) the minimum scalar variance in Figure 8. A flow time of $t/\tau = 16$ occurs after the initial Kelvin-Helmholtz rollup with dominant two-dimensional structures and near-uniform mixed-fluid composition, as shown in Figures 2(a)-2(b), whereas the flow field at $t/\tau = 80$ is highly three-dimensional, characterized by a less-uniform mixed-fluid composition, as shown in Figure 2(c). Figure 11 shows the mid-plane scalar PDF at those times. As expected, the probability of finding mixed-fluid at the mid-plane is higher with the TVD scheme at $t/\tau = 16$ because of its numerical diffusivity, but once the fluid around the mid-plane is mixed, numerical (or molecular) diffusivity plays a negligible role in the mixed-fluid composition evolution and both schemes yield similar behavior at $t/\tau = 80$. Figures 9, 10, and 11 show results from the stretched-vortex SGS model. Similar results from the dynamic-Smagorinsky SGS model are omitted for brevity.

Accurate estimates of mixed-fluid composition are critical in reacting-flow simulations, since errors will yield incorrect predictions of product formation and heat release [67]. A method to estimate the numerical-dissipation influence on heat release in such flows, obviating solution of the reacting-flow equations, is proposed in Appendix C.

4.2.3. Subgrid scalar variance and dissipation

The previous section discusses the resolved scalar variance and the numerical-dissipation influence on it. The stretched-vortex SGS model allows an estimate of subgrid contributions to the total scalar variance and dissipation (see Section 2.1), which enables a comparison between the subgrid contributions and numerical-dissipation errors.

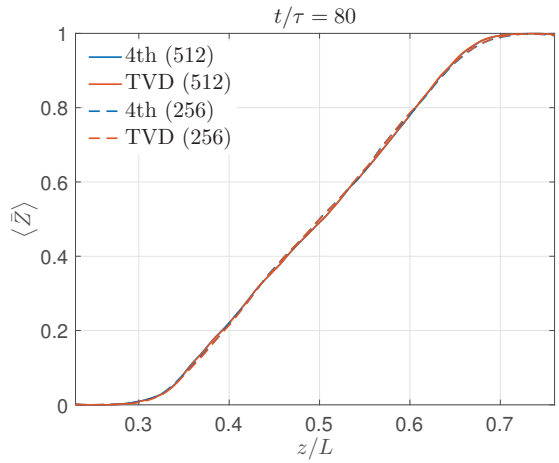

Figure 9: Local mean, $\langle \bar{Z} \rangle$, of the scalar concentration across the shear-layer width at $t/\tau = 80$ using the stretched-vortex SGS model. Parentheses in legend denote the number of grid points in each direction, N.

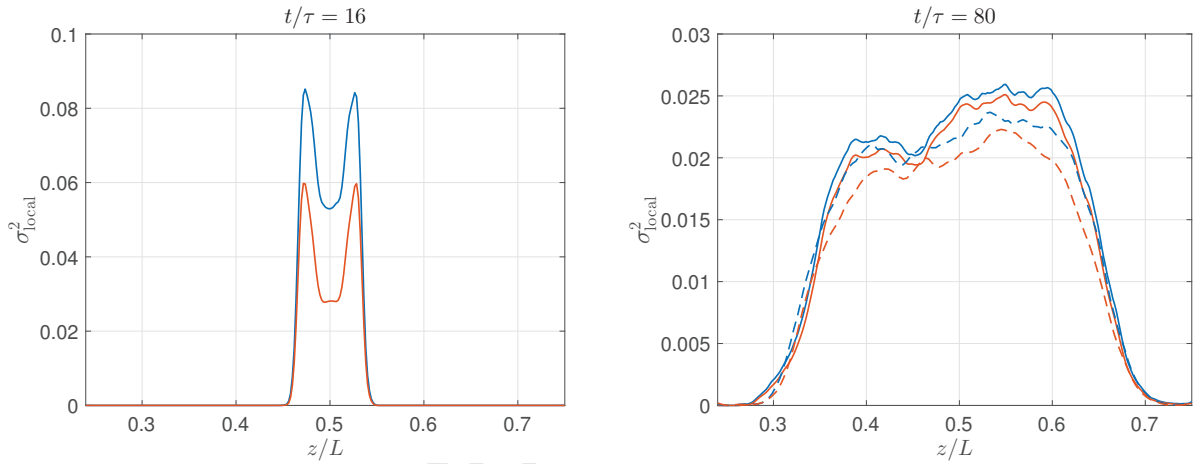

Figure 10: Comparison of resolved local scalar variance between the solution from the fourth-order non-dissipative and the TVD scheme at (a) $t/\tau = 16$, (b) $t/\tau = 80$ using the stretched-vortex SGS model. Legend same as in Figure 11.

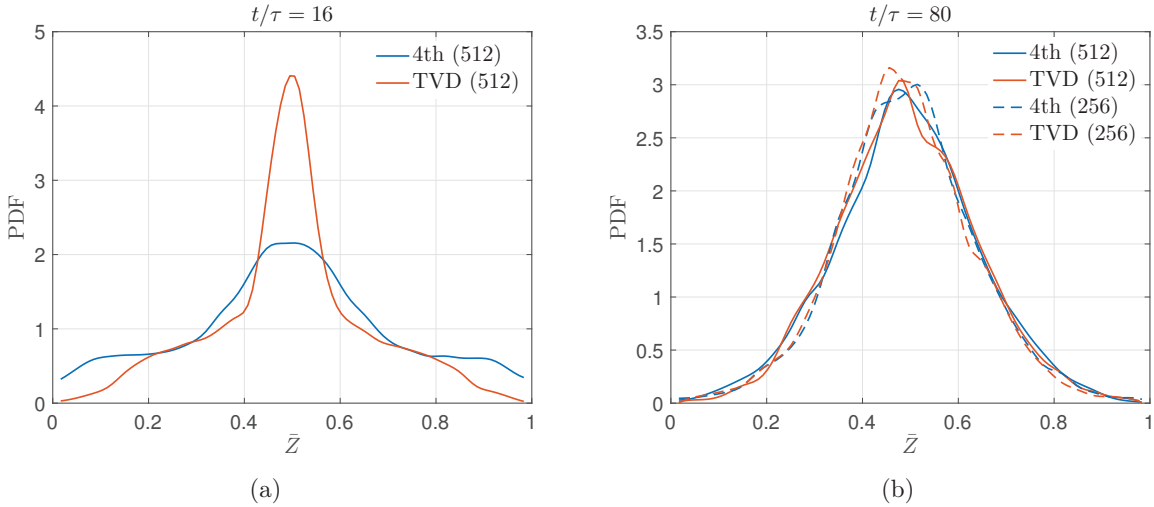

Figure 11: Comparison of the resolved mid-plane scalar PDF at (a) $t/\tau = 16$, (b) $t/\tau = 80$ using the stretched-vortex SGS model. Parentheses in legend denote the number of grid points in each direction, N.

Total scalar variance, following [31, Eq. (4.4)], can be estimated from

$$\sigma^2_{\text{tot}} = \int_{-\delta_Z/2}^{\delta_Z/2} \left\langle Z'^2 \right\rangle \, \mathrm{d}z, \tag{30}$$

where, with mild assumptions, $\left\langle Z'^2 \right\rangle \approx \left\langle \bar{Z}'^2 \right\rangle + \left\langle \sigma^2_{\text{sub}} \right\rangle$. $\bar{Z}' = \bar{Z} - \left\langle \bar{Z} \right\rangle$ is the resolved scalar fluctuation such that $\left\langle \bar{Z}'^2 \right\rangle = \sigma^2_{\text{local}}$, shown in Figure 10, and σ^2_{sub} is estimated from Eq. (6).

Similarly, total scalar dissipation can be estimated from

$$\varepsilon_{\text{tot}} = \int_{-\delta_Z/2}^{\delta_Z/2} \left\langle \epsilon_{\text{s}} \right\rangle \, \mathrm{d}z, \tag{31}$$

where $\epsilon_s = \mathcal{D}\left(\partial \bar{Z}/\partial x_j\right)^2 + \epsilon_{\text{sub}}$. Subgrid scalar dissipation in each cell, ϵ_{sub}, is estimated by Eq. (5), such that $\varepsilon_{\text{sgs}} = \int_{-\delta_Z/2}^{\delta_Z/2} \left\langle \epsilon_{\text{sub}} \right\rangle \, \mathrm{d}z$ and, similarly, $\sigma^2_{\text{sgs}} = \int_{-\delta_Z/2}^{\delta_Z/2} \left\langle \sigma^2_{\text{sub}} \right\rangle \, \mathrm{d}z$.

Figure 12 shows the total scalar variance and dissipation, denoted Total, as well as the subgrid contribution to these quantities, denoted SGS, for solutions from the non-dissipative fourth-order and the dissipative TVD scheme for $N = 256$ and 512. The initial resolved scalar field, (13), is unperturbed and, therefore, the subgrid variance accounts for all the variance at initial time in Figure 12(a). Subgrid variance from the non-dissipative scheme accounts for around 15% of the total variance in the development stage of flow and around $6\% - 8\%$ of the total variance at late times, whereas, subgrid variance from the TVD scheme accounts for only 5% in the development stage and around $2\% - 3\%$ at late times. The y-axis in Figure 12(a) is logarithmic to highlight the difference of subgrid contributions from the two schemes.

The difference in total variance between the two schemes, i.e., the error attributable to numerical dissipation, decreases with time but exceeds the subgrid contribution from either scheme at all times. As expected, the subgrid variance on the coarser grid is higher and the total variance is roughly the same for the two grid resolutions. The subgrid contribution to the total scalar dissipation, shown in Figure 12(b), accounts for roughly all the dissipation at both grid resolutions. Total scalar dissipation calculated from the solution of the TVD scheme is roughly half of that from the non-dissipative scheme. The difference is a consequence of higher spatial fluctuations in the scalar field from the non-dissipative scheme, as discussed in Appendix D, which results in higher SGS dissipation (proportional to the square of scalar gradients).

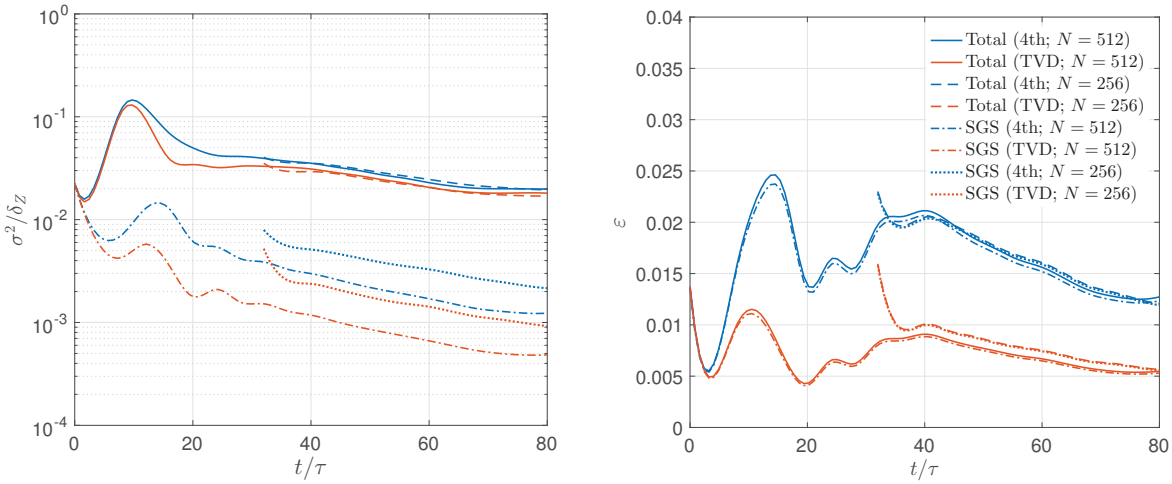

Figure 12: (a) Total ($\sigma^2_{\text{tot}}/\delta_Z$) and subgrid ($\sigma^2_{\text{sgs}}/\delta_Z$) scalar variance, (b) Total (ε_{tot}) and subgrid (ε_{sgs}) dissipation from the fourth-order non-dissipative and the TVD scheme for the scalar-convection term discretization. N denotes the number of grid points in each direction. Legend is the same for both plots.

4.3. Bounded-scheme results

Section 3 discusses approaches to mitigate unphysical scalar excursions with finite-volume and finite-difference schemes. The linear-scaling limiter of [22, 23] is used for finite-volume schemes, whereas the monotonicity-preserving limiter of [24] for finite-difference schemes. In this section, we analyze results from the application of the bounded finite-volume approach of Section 3.1 to WENO(D)-opt and WENO4-opt schemes (see Appendix B) and the bounded finite-difference approach of Section 3.2 to the fourth-order non-dissipative scheme of [25]. We choose the three schemes because of their low dissipation errors. However, any other numerical scheme as discussed in Section 3 could also be used.

Prefixes "L-" and "MP-" denote schemes with the linear-scaling and the monotonicity-preserving limiter, respectively. $N = 256$ is used for all simulations. Global scalar-excursion statistics from the schemes with and without limiters are shown in Table 3 and Figure 13. Table 3 shows the volume fractions (scaled by the factors in the Multiplier column) of threshold violation given in Column 1. Figure 13 shows the maximum and minimum scalar value from different schemes with time. As evident, both limiters eliminate all overshoots and undershoots.

Scalar spectra can help assess numerical dissipation introduced by the limiters. Figure 14 shows the one-dimensional scalar and scalar-gradient spectra along the streamwise direction on the mid-plane $\left(\langle \bar{Z} \rangle = 0.5\right)$ at $t/\tau = 80$ from different schemes with and without the limiters. The limited-scheme results are shown by dot-dashed lines. They follow the corresponding solid lines closely in each case, indicating that very little dissipation is introduced by both limiters at mid-plane. The scalar concentration on the mid-plane at $t/\tau = 80$, as shown in Figure 11(b), is expected to be around 0.5, therefore, the effect of bound-preserving limiters, which act around the physical bounds of 0 and 1, is expectedly minimal. To examine the effect at other planes, Figures 15(a) and 15(b) plot the scalar spectra on planes $z/\delta_Z = 0.2$ $\left(\langle \bar{Z} \rangle = 0.7\right)$ and $z/\delta_Z = 0.4$ $\left(\langle \bar{Z} \rangle = 0.94\right)$, respectively. The limited finite-volume schemes, L-WENO(D)-opt and L-WENO4-opt, show little deviation from the corresponding non-limited scheme results, indicating that very little additional dissipation is introduced by the limiters. The deviation is slightly higher for the monotonicity-preserving limiter applied to the non-dissipative fourth-order scheme at $z/\delta_Z = 0.4$, which may partly be a result of the suppression of unphysical scalar variance from overshoots and undershoots.

In Section 4.2.2, the mid-plane scalar PDF and scalar variance were found to be sensitive to numerical dissipation in the development stage of the shear flow. Figure 16 shows those results for schemes with and without the limiters, demonstrating that the difference in mixed-fluid composition traceable to additional dissipation from the limiting approaches is minimal.

Table 4 shows the CPU time per iteration, overhead with respect to the TVD scheme, and the fraction of total run time expended in scalar-convection-term evaluation from different schemes, determined using the profiling tool gprof [68]. The total and scalar-convection CPU times per iteration are calculated by averaging over 100 iterations the total compute time and the time spent in subroutines evaluating scalar-convection-term, respectively, in a serial execution. All computations are carried out on a workstation with Intel Xeon CPU E5-2670 processor using intel compiler (version 17.0.1) and compiler options `-o3 -r8` for optimization and double precision. CPU times are sensitive to the choice of compiler and optimization flags but overheads with respect to a given scheme and percentages of total run time are similar. Since the bound-preserving limiters act only in case of scalar overshoots/undershoots, the computational expense depends on the flow characteristics. Flows with sharper gradients near global bounds, expected to produce more overshoots/undershoots, will have more calls to the limiter subroutine in the program run and entail higher cost. The compute times presented in Table 4 are calculated from runs around the flow time $t/\tau \approx 60$, when the computational domain has nearly equal mixed and unmixed fluid. As evident from the table, MP-4th is approximately three times more expensive than the non-dissipative fourth-order scheme, but because of small fraction of total run time required for scalar-convection-term evaluation, the relative influence on total CPU time/iteration is small. WENO schemes are expectedly more expensive than the non-dissipative fourth-order and TVD scheme.

Scalar value	Volume fraction						
	Multiplier	Scalar-convection scheme					
		4th	MP-4th	WENO(D) -opt	L-WENO(D) -opt	WENO4 -opt	L-WENO4 -opt
> 1.01	10^{-2}	2.009	0	1.357	0	1.369	0
> 1.02	10^{-2}	1.074	0	0.465	0	0.472	0
> 1.05	10^{-3}	2.308	0	0.189	0	0.192	0
> 1.1	10^{-4}	2.709	0	0.009	0	0.008	0
> 1.2	10^{-6}	5.782	0	0	0	0	0
$<$ -0.01	10^{-2}	2.147	0	0.208	0	0.218	0
$<$ -0.02	10^{-2}	1.182	0	0.036	0	0.041	0
$<$ -0.05	10^{-3}	2.583	0	0.003	0	0.003	0
$<$ -0.1	10^{-4}	2.629	0	0	0	0	0
$<$ -0.2	10^{-6}	2.921	0	0	0	0	0

Table 3: Global scalar excursion statistics at $t/\tau = 80$ from different numerical schemes applied to the scalar-convection term.

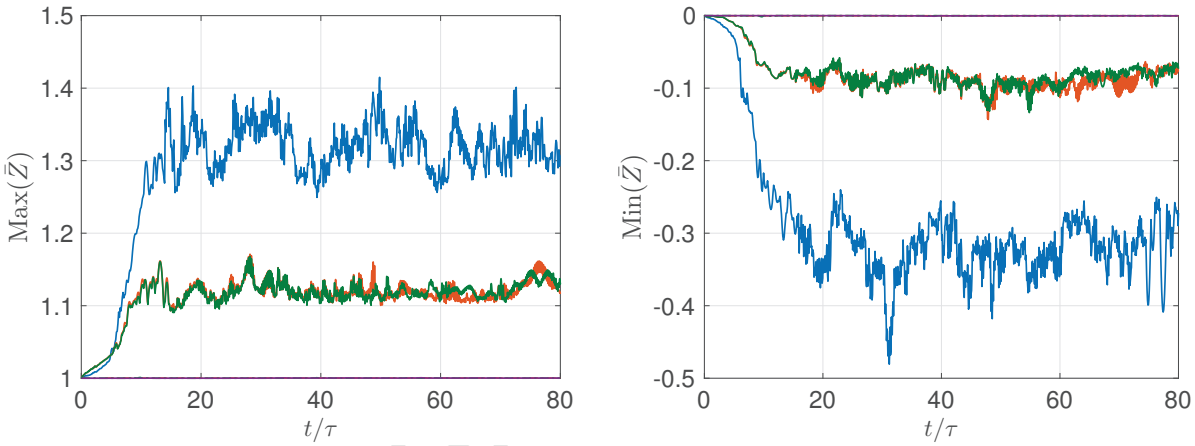

(a) (b)

Figure 13: Global scalar excursion in simulations using different numerical schemes. (a) Maximum overshoot, (b) Maximum undershoot. Legend same as in Figure 14.

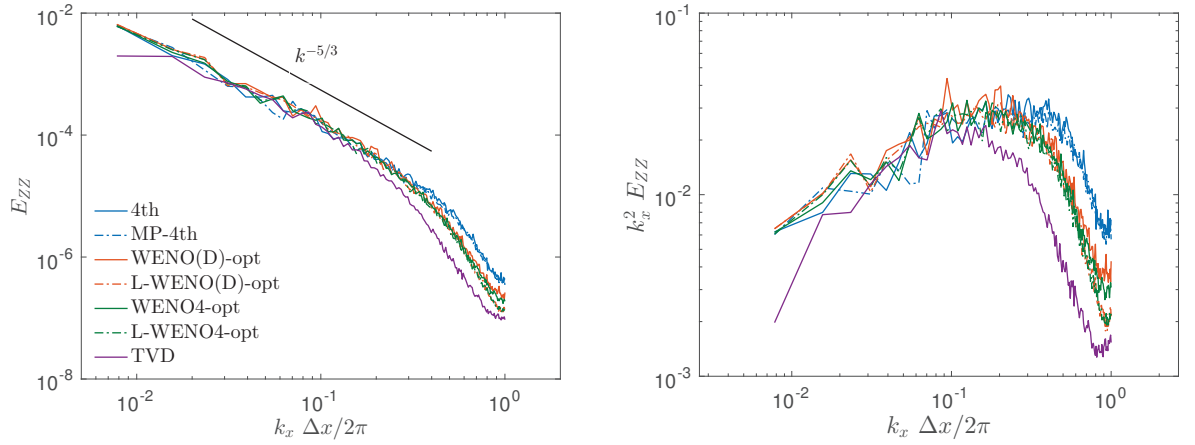

(a) (b)

Figure 14: One-dimensional spectra along the streamwise direction on the mid-plane of mixing layer at $t/\tau = 80$. (a) Scalar spectra, E_{ZZ}, (b) Scalar gradient spectra $k_x^2 E_{zz}$.

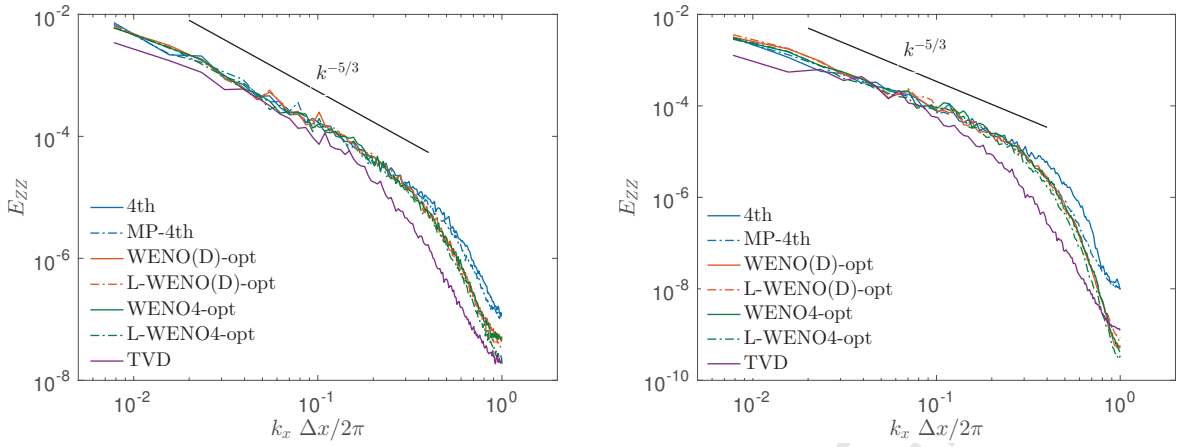

Figure 15: One-dimensional scalar spectra along the streamwise direction at $t/\tau = 80$ on horizontal planes: (a) $z/\delta_Z = 0.2$, and (b) $z/\delta_Z = 0.4$, where the shear-layer extent is $z/\delta_Z \in [-0.5, 0.5]$.

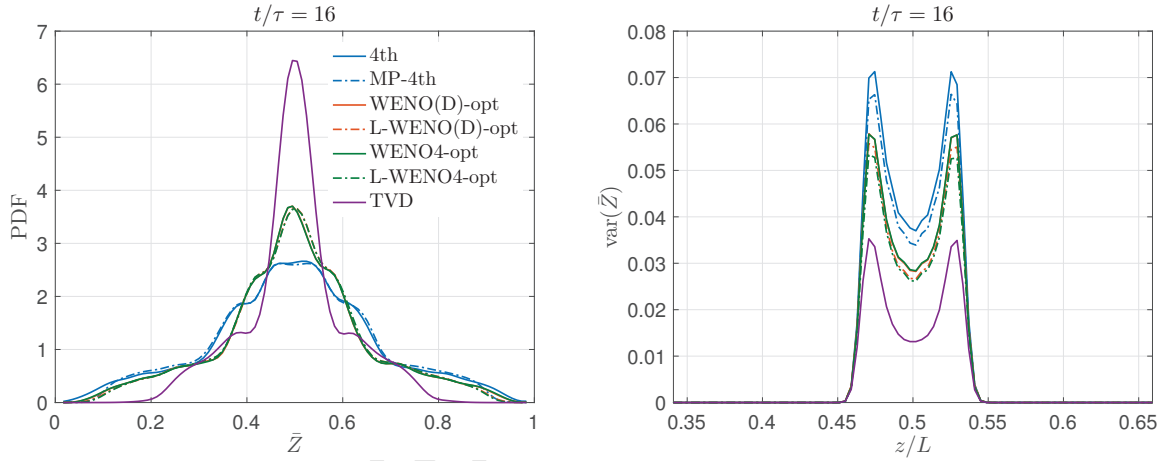

Figure 16: (a) Mid-plane scalar PDF and (b) local scalar variance at $t/\tau = 16$ from different schemes with and without limiters. Legend is the same for both plots.

	Scalar-convection			Total
Scheme	CPU time/iteration (s)	Overhead w.r.t. TVD	% of total run time	CPU time/iteration (s)
4th	0.636	1.43	4.2	15.242
MP-4th	1.850	4.16	11.2	16.459
WENO(D)-opt	6.542	14.73	30.9	21.148
L-WENO(D)-opt	8.774	19.74	37.5	23.380
WENO4-opt	3.615	8.14	19.8	18.222
L-WENO4-opt	7.482	16.84	33.9	22.089
TVD	0.445	1.00	3.0	15.050

Table 4: Computational cost of different schemes using $N = 128$ and a CFL number of 0.3 for all cases.

In summary, mixing sensitivity to numerical dissipation is flow-dependent, as might be expected. The shear flow considered here, described in Section 2.2, evolves through different mixing phases, which allows a study across various mixing regimes. Figure 8 shows a higher sensitivity to numerical dissipation in the

development stage of the flow and the over-diffusive nature of the stretched-vortex SGS model on coarser grid. To study the long-time mixing evolution, the fine-grid simulation was extended, allowing shear layers in the periodic configuration to merge and homogenize. Figure 17 compares the global scalar-variance between the non-dissipative fourth-order and the TVD scheme for a long-time simulation. It highlights higher sensitivity at early times, which, as expected, diminishes as the flow field approaches momentum and scalar homogenization. The time of local maximum and minimum in scalar variance, however, is unaffected by the additional dissipation. The time axis in Figure 8 is logarithmic to compress the much-longer times involved and help scale the approach of the flow to the asymptotic homogenized state.

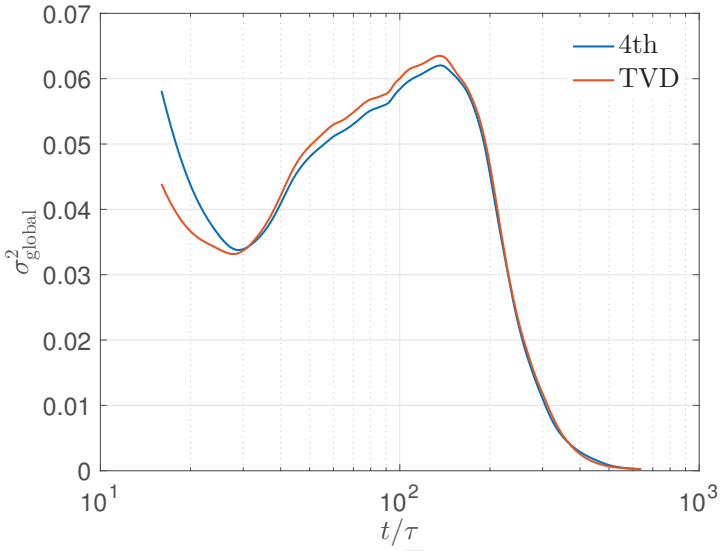

Figure 17: Resolved global scalar-variance comparison between the non-dissipative fourth-order and the TVD scheme for a long-time simulation using $N = 512$. Note the logarithmic time axis.

5. Conclusions

LES of incompressible temporally evolving shear flow using the stretched-vortex and the dynamic-Smagorinsky SGS model examine the effects of numerical dissipation on scalar mixing, introduced in mitigating unphysical scalar excursions. The sensitivity of the shear flow to initial conditions is exploited to generate flows with different mixed-fluid compositions across shear layer, enabling a study of numerical-dissipation influence in different mixing regimes, and the time of transition between them. TVD schemes ensure scalar boundedness but are known to be too dissipative. An assessment of mixed-fluid composition in different stages of the shear flow evolution shows that numerical dissipation from a TVD scheme enhances mixing in all stages of the flow, exhibiting much higher sensitivity in the development stage characterized by organized large-scale flow-structure interactions and near-uniform mixed-fluid composition, but does not alter the character of the mixed-fluid composition (uniform vs. non-uniform) as well as the time of transition between mixing regimes and the time when local extrema in scalar variance are attained.

Additional dissipation influences scalar-field behavior at small scales and, therefore, statistics driven by large-scale structures, such as mixing-zone width and growth rate, are less sensitive to numerical dissipation. Mid-plane scalar PDF and local scalar variance are sensitive to numerical dissipation in the development stage of the flow but less so at late times. Total scalar variance and dissipation show sensitivity to numerical dissipation in all stages of the flow evolution. They provide useful diagnostic metrics to assess dissipation attributable to mitigation techniques for unphysical scalar excursions.

Two approaches based on flux reconstruction, using a linear-scaling limiter for finite-volume schemes and a monotonicity-preserving limiter for finite-difference schemes, are presented for scalar boundedness in incompressible-flow simulations. Both approaches eliminate unphysical scalar excursions with minimal dissipation and preserve design order of accuracy with a conservative discretization. They provide better alternatives to TVD schemes for scalar boundedness in turbulent-flow simulations. For the incompressible shear flow considered here, MP-4th is a suitable scalar-convection scheme. It introduces minimal numerical dissipation, as shown in Figures 14-16, and eliminates the overshoots/undershoots, as shown in Table 3 and Figure 13.

Acknowledgements

This work was supported by the Department of Energy/National Nuclear Security Administration Award number DE-NA0002382 and the AFOSR Grant FA9550-12-1-0461. The authors would also like to acknowledge computing support by Dr. Daniel Lang and discussions with Prof. C. Pantano at the University of Illinois, Prof. G. Candler at the University of Minnesota, and Prof. D. Meiron and Prof. D. Pullin at Caltech.

Appendix A. WENO-scheme implementation on staggered grid

For the incompressible flow simulations discussed in this paper, Eq. (2) is solved on a staggered grid, where scalar values are stored at the cell center and velocity components at the cell edges in 2D (cell faces in 3D), as shown in Figure 4. A conservative discretization is used for the scalar-convection term, such that for $f = \bar{u}\bar{Z}$,

$$\left.\frac{\partial f}{\partial x}\right|_i \approx \frac{f_{i+\frac{1}{2}} - f_{i-\frac{1}{2}}}{\Delta x}, \tag{A.1}$$

and, similarly, for the fluxes in the y- and z-direction. The flux at a cell interface is $f_{i+\frac{1}{2}} = \hat{f}\left(\bar{Z}^L_{i+\frac{1}{2}}, \bar{Z}^R_{i+\frac{1}{2}}, \bar{u}_{i+\frac{1}{2}}\right)$. Velocity components, calculated from the momentum equation, are stored at cell interfaces, therefore, no reconstruction is performed for $\bar{u}_{i+\frac{1}{2}}$, and WENO reconstructions are applied only to the scalar field to obtain $\bar{Z}^{L,R}_{i+\frac{1}{2}}$. The cell-interface flux is then obtained from the left and the right state using the upwind flux given by Eq. 24.

The performance of three WENO schemes is analyzed in Sections 4.1 and 4.3 for the the LES of turbulent shear flow. Here, we conduct Taylor-Green vortex flow simulations with passive scalar transport to assess the convergence of the three schemes on a staggered grid with the implementation described above. The flow is governed by the incompressible (uniform-density) Navier-Stokes equations, i.e., (2) without the SGS terms. The analytical solution is given by

$$u(x,y,t) = -\cos(x)\sin(y)\,e^{-2\nu t}, \qquad v(x,y,t) = -\sin(x)\cos(y)\,e^{-2\nu t},$$

$$w(x,y,t) = 0, \qquad Z(x,y,t) = -\cos(x)\cos(y)\,e^{-2\nu t/Sc},$$

where $\nu = 0.025$ and $Sc = 1.0$ is assumed. Table A.5 shows the accuracy of different WENO schemes with errors calculated at $t = 2.0$. A small enough time step is chosen so that temporal errors are much smaller than spatial truncation errors. The momentum-equation terms and the viscous term of the scalar equation are discretized using the sixth-order centered scheme to isolate the errors from the scalar-field WENO reconstruction. All schemes exhibit the design order of accuracy. A higher convergence rate with WENO4 ($r = 3$ scheme of Liu *et al.* [51]), which is expected to be fourth-order accurate, is because of larger errors on coarser grids, as pointed in [52] and confirmed in Table A.5.

$N \times N$	WENO(D)		WENO5		WENO4	
	L_2 error	Order	L_2 error	Order	L_2 error	Order
64×64	5.57e-07		3.90e-06		5.96e-05	
128×128	1.68e-08	5.053	1.21e-07	5.012	2.64e-06	4.496
256×256	4.94e-10	5.084	3.57e-09	5.078	9.37e-08	4.817
512×512	1.43e-11	5.112	9.57e-11	5.224	2.19e-09	5.419

Table A.5: L_2 error and convergence rate of different WENO schemes for Taylor-Green vortex flow solved on a staggered grid.

Appendix B. Comparison of WENO schemes with different smoothness estimator

In this appendix, the global scalar-excursion statistics and scalar spectra (indicators of the dispersion and dissipation properties of a numerical scheme, respectively) are compared between the WENO schemes with solution-dependent and optimal weights. For smooth flow fields, such as the mixing layer analyzed in this paper, the solution-dependent weights in the WENO schemes are found to be excessively diffusive, and the optimal weights are better suited. Other variants of WENO schemes that add a downwind stencil [69], or adapt the solution-dependent weights to map to optimal values faster [70, 71], or do both [72] to reduce numerical dissipation are not considered here. Instead, smooth flow fields in the turbulent shear flow considered here allows use of optimal weights in all cells. The optimal weights can be found in [51, Section 3.6] for the WENO4 and [52, Table 2] for the WENO5 scheme. For WENO(D), the weights, λ, are assumed to be zero for one-sided stencils in [50, Section 2.2], i.e., only the central stencil is used.

Table B.6 and Figure B.18 show the global scalar-excursion statistics from WENO schemes, discussed in Section 4.1, with optimal weights, denoted by the suffix "-opt". No suffix denotes the classical approach with solution-dependent weights. Figure B.19 compares the one-dimensional scalar and scalar-gradient spectra, along the streamwise direction on the mid-plane, between them. As expected, optimal weights introduce less dissipation but cause higher unphysical scalar excursions.

Scalar value	Volume fraction							
	Multiplier	Scalar-convection scheme						
		4th	WENO4 -opt	WENO4	WENO5 -opt	WENO5	WENO(D) -opt	WENO(D)
> 1.01	10^{-2}	2.009	1.369	0.192	1.355	0.299	1.357	0.738
> 1.02	10^{-2}	1.074	0.472	0.024	0.468	0.038	0.465	0.180
> 1.05	10^{-3}	2.308	0.192	0.003	0.197	0.003	0.189	0.035
> 1.1	10^{-4}	2.709	0.008	0	0.008	0	0.009	0.0006
> 1.2	10^{-6}	5.782	0	0	0	0	0	0
$<$ -0.01	10^{-2}	2.147	0.218	0	0.209	0	0.208	0.0001
$<$ -0.02	10^{-2}	1.182	0.041	0	0.037	0	0.036	0
$<$ -0.05	10^{-3}	2.583	0.003	0	0.003	0	0.003	0
$<$ -0.1	10^{-4}	2.629	0	0	0	0	0	0
$<$ -0.2	10^{-6}	2.921	0	0	0	0	0	0

Table B.6: Global scalar-excursion statistics at $t/\tau = 80$ from different numerical schemes applied to the scalar-convection term, and $N = 256$.

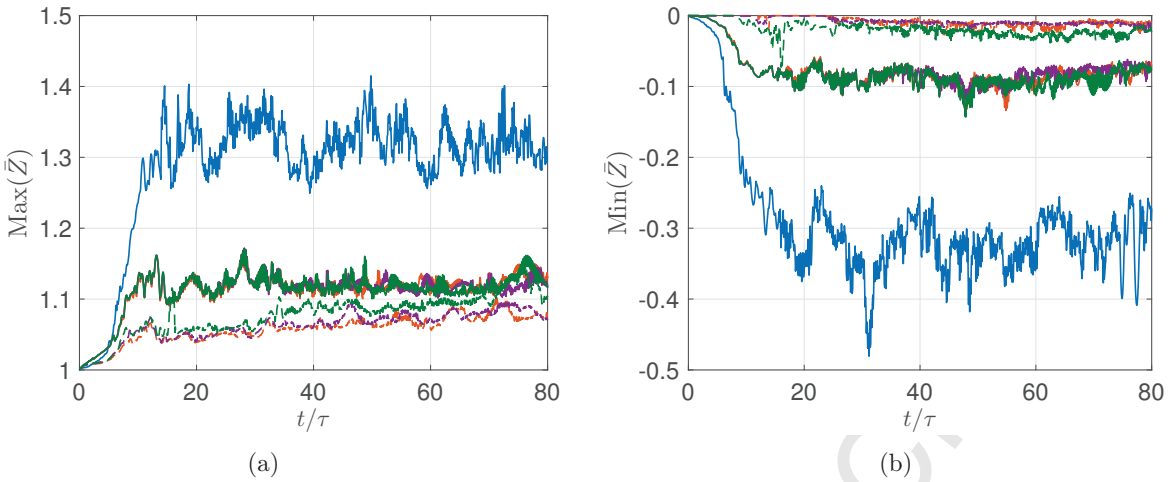

(a) (b)

Figure B.18: Global scalar excursion from different numerical schemes using $N = 256$. (a) Maximum overshoot, (b) Maximum undershoot. Legend same as in Figure B.19(a).

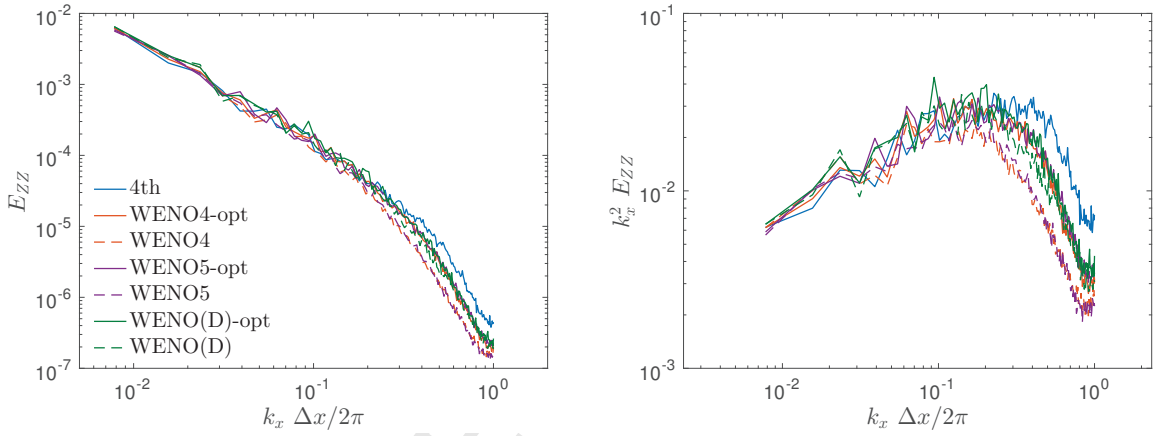

(a) (b)

Figure B.19: One-dimensional spectra along the streamwise direction on the mid-plane of mixing layer at $t/\tau = 80$ using $N = 256$. (a) Scalar spectra, E_{ZZ}, (b) Scalar gradient spectra $k_x^2 E_{ZZ}$.

Appendix C. Estimate of numerical-dissipation influence on heat release

Normalized temperature rise $\Delta\bar{T}(z;\phi)/\Delta T_f$ in the limit of fast chemistry can be written as (e.g., [73])

$$\frac{\Delta\bar{T}(z;\phi)}{\Delta T_f} = \int_0^1 Y_p(\bar{Z}, Z_\phi)\mathcal{P}(\bar{Z};z)\,\mathrm{d}\bar{Z},$$

where $\mathcal{P}(\bar{Z};z)$ denotes the resolved-scalar PDF at a horizontal plane and ΔT_f is the adiabatic flame temperature rise. $Y_p(\bar{Z}, Z_\phi)$ is the product produced corresponding to a particular mixture fraction assuming complete consumption of lean reactant,

$$Y_p(\bar{Z}, Z_\phi) = \begin{cases} \frac{\bar{Z}}{Z_\phi} & \text{for} \quad 0 \le \bar{Z} \le Z_\phi, \\ \frac{1-\bar{Z}}{1-Z_\phi} & \text{for} \quad Z_\phi \le \bar{Z} \le 1. \end{cases}$$

For a stoichiometric mixture ratio ϕ, complete consumption of all reactants occurs at a stoichiometric-mixture mole fraction,

$$Z_\phi = \frac{\phi}{\phi + 1}.$$

Consider the chemical reaction between hydrogen and fluorine in the limit of fast chemistry [73],

$$H_2 + F_2 \rightarrow 2HF \quad .$$

Figure C.20 compares the normalized temperature rise for H_2-rich ($\phi = 1/8$) condition at times used in Figures 10 and 11 between the fourth-order non-dissipative and the TVD scheme. Consistent with the observations in Figures 10 and 11, a higher normalized temperature rise in Figure C.20(a) from the TVD scheme indicates a greater chemical-product volume fraction, and is a result of higher estimated mixing because of numerical diffusivity. A longer time allows homogenization by large-scale flow structures and the two schemes yield similar results at $t/\tau = 80$, as shown in Figure C.20(b).

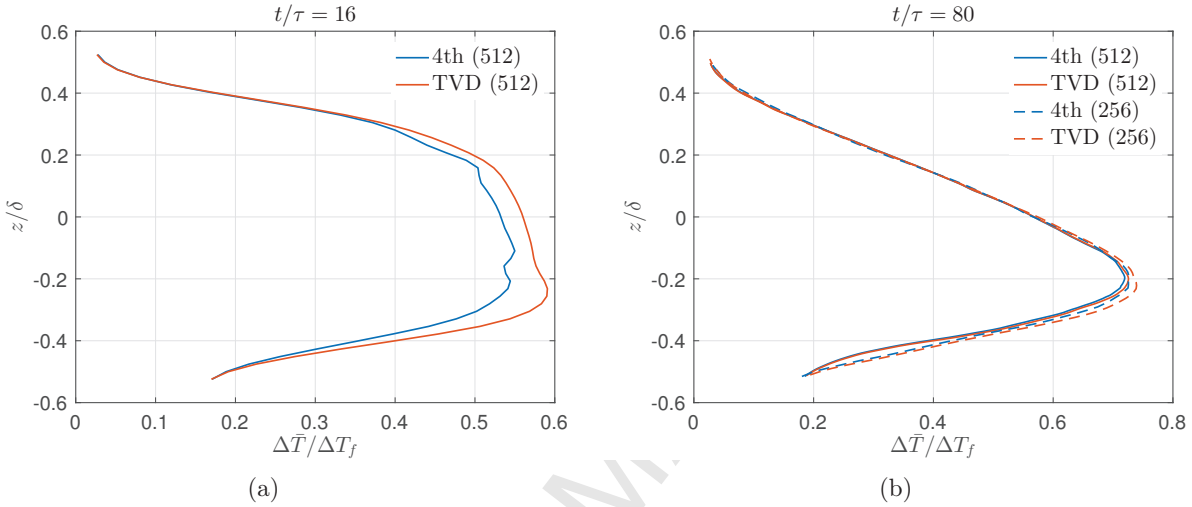

Figure C.20: Comparison of the normalized temperature rise for H_2-rich ($\phi = 1/8$) condition at (a) $t/\tau = 16$, (b) $t/\tau = 80$.

Appendix D. Point-wise comparison of the scalar field

In this appendix, we discuss the point-wise difference of the scalar field obtained from schemes with different numerical dissipation. Figure D.21 shows contours of the scalar field at the $y = 0$ plane from the fourth-order non-dissipative and the flux-limited TVD scheme at $t/\tau = 80$. The diffusive nature of the TVD scheme is evident from a comparison of the fine-structure resolution between Figures D.21(a) and D.21(b). Figures D.22(a) and D.22(b) plot scalar values along the vertical line $x = 0$ of Figure D.21 and a horizontal line at the shear layer mid-plane, respectively. The plots highlight some of the observations made in Sections 4.1 and 4.2. Global scalar excursions from the non-dissipative fourth-order scheme can be seen as overshoots and undershoots in Figure D.22(a), whereas the TVD scheme observes boundedness. Scalar fluctuations in Figure D.22 are higher for the non-dissipative scheme and, therefore, its scalar variance (discussed in Section 4.2.2) is also higher.

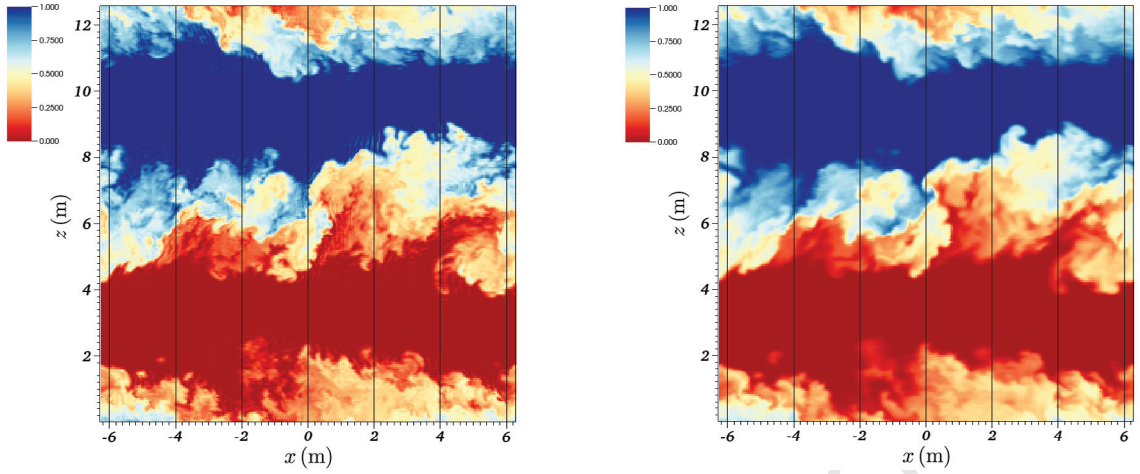

(a) (b)

Figure D.21: Contours of the scalar field at the $y = 0$ plane from the (a) non-dissipative fourth-order scheme, (b) TVD scheme at $t/\tau = 80$, using $N = 256$. The extent of the computational domain (in m): $x, y \in [-2\pi, 2\pi]$ and $z \in [0, 4\pi]$.

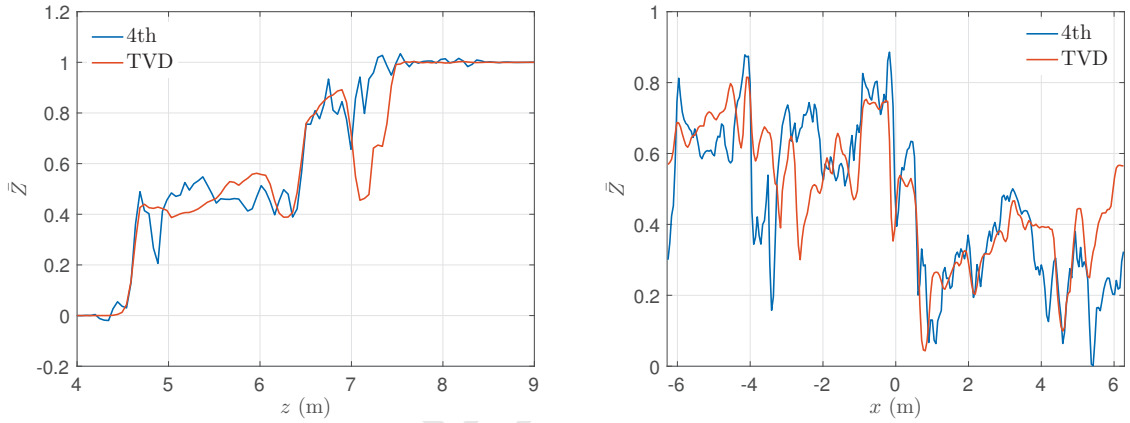

(a) (b)

Figure D.22: Point-wise scalar values at $t/\tau = 80$ along (a) the vertical line: $x = 0\,\mathrm{m}$, $y = 0\,\mathrm{m}$, (b) the horizontal line: $y = 0\,\mathrm{m}$, $z = 2\pi\,\mathrm{m}$, from simulations using $N = 256$.

[1] B. I. Shraiman, E. D. Siggia, Scalar turbulence, Nature 405 (6787) (2000) 639–646.

[2] Z. Warhaft, Passive scalars in turbulent flows, Annual Review of Fluid Mechanics 32 (1) (2000) 203–240.

[3] P. E. Dimotakis, Turbulent mixing, Annu. Rev. Fluid Mech. 37 (2005) 329–356.

[4] P. Sagaut, Large eddy simulation for incompressible flows: an introduction, Springer Science & Business Media, 2006.

[5] E. Garnier, N. Adams, P. Sagaut, Large eddy simulation for compressible flows, Springer Science & Business Media, 2009.

[6] B. Vreman, B. Geurts, H. Kuerten, Comparison of numerical schemes in large-eddy simulation of the temporal mixing layer, International Journal for Numerical Methods in Fluids 22 (4) (1996) 297–311.

[7] B. J. Geurts, Balancing errors in les, in: Direct and Large-Eddy Simulation III, Springer, 1999, pp. 1–12.

[8] J. Meyers, B. J. Geurts, M. Baelmans, Database analysis of errors in large-eddy simulation, Physics of Fluids 15 (9) (2003) 2740–2755.

[9] B. J. Geurts, Interacting errors in large-eddy simulation: a review of recent developments, Journal of Turbulence (7) (2006) N55.

[10] F. K. Chow, P. Moin, A further study of numerical errors in large-eddy simulations, Journal of Computational Physics 184 (2) (2003) 366–380.

[11] J. Gullbrand, F. K. Chow, The effect of numerical errors and turbulence models in large-eddy simulations of channel flow, with and without explicit filtering, Journal of Fluid Mechanics 495 (2003) 323–341.

[12] B. J. Geurts, J. Fröhlich, A framework for predicting accuracy limitations in large-eddy simulation, Physics of fluids 14 (6) (2002) L41–L44.

[13] K. Horiuti, Comparison of conservative and rotational forms in large eddy simulation of turbulent channel flow, Journal of Computational Physics 71 (2) (1987) 343–370.

[14] A. Kravchenko, P. Moin, On the effect of numerical errors in large eddy simulations of turbulent flows, Journal of Computational Physics 131 (2) (1997) 310–322.
[15] S. Ghosal, An analysis of numerical errors in large-eddy simulations of turbulence, Journal of Computational Physics 125 (1) (1996) 187–206.
[16] P. J. Mason, Large-eddy simulation: A critical review of the technique, Quarterly Journal of the Royal Meteorological Society 120 (515) (1994) 1–26.
[17] G. Matheou, P. E. Dimotakis, Scalar excursions in large-eddy simulations, Journal of Computational Physics 327 (2016) 97–120.
[18] M. Herrmann, G. Blanquart, V. Raman, Flux corrected finite volume scheme for preserving scalar boundedness in reacting large-eddy simulations, AIAA journal 44 (12) (2006) 2879–2886.
[19] S. Muppidi, K. Mahesh, Direct numerical simulation of passive scalar transport in transverse jets, Journal of Fluid Mechanics 598 (2008) 335–360.
[20] S. Verma, Y. Xuan, G. Blanquart, An improved bounded semi-lagrangian scheme for the turbulent transport of passive scalars, Journal of Computational Physics 272 (2014) 1–22.
[21] P. K. Subbareddy, A. Kartha, G. V. Candler, Scalar conservation and boundedness in simulations of compressible flow, Journal of Computational Physics 348 (2017) 827–846.
[22] X.-D. Liu, S. Osher, Nonoscillatory high order accurate self-similar maximum principle satisfying shock capturing schemes i, SIAM Journal on Numerical Analysis 33 (2) (1996) 760–779.
[23] X. Zhang, C.-W. Shu, On maximum-principle-satisfying high order schemes for scalar conservation laws, Journal of Computational Physics 229 (9) (2010) 3091–3120.
[24] A. Suresh, H. Huynh, Accurate monotonicity-preserving schemes with runge–kutta time stepping, Journal of Computational Physics 136 (1) (1997) 83–99.
[25] Y. Morinishi, T. S. Lund, O. V. Vasilyev, P. Moin, Fully conservative higher order finite difference schemes for incompressible flow, Journal of computational physics 143 (1) (1998) 90–124.
[26] A. Leonard, Energy cascade in large-eddy simulations of turbulent fluid flows, Advances in geophysics 18 (1975) 237–248.
[27] T. Lund, The use of explicit filters in large eddy simulation, Computers & Mathematics with Applications 46 (4) (2003) 603–616.
[28] A. Misra, D. I. Pullin, A vortex-based subgrid stress model for large-eddy simulation, Physics of Fluids 9 (8) (1997) 2443–2454.
[29] D. I. Pullin, A vortex-based model for the subgrid flux of a passive scalar, Physics of Fluids 12 (9) (2000) 2311–2319.
[30] D. Hill, C. Pantano, D. Pullin, Large-eddy simulation and multiscale modelling of a richtmyer–meshkov instability with reshock, Journal of fluid mechanics 557 (2006) 29–61.
[31] T. Mattner, Large-eddy simulations of turbulent mixing layers using the stretched-vortex model, Journal of Fluid Mechanics 671 (2011) 507–534.
[32] D. Pullin, T. Lundgren, Axial motion and scalar transport in stretched spiral vortices, Physics of Fluids 13 (9) (2001) 2553–2563.
[33] M. Germano, U. Piomelli, P. Moin, W. H. Cabot, A dynamic subgrid-scale eddy viscosity model, Physics of Fluids A: Fluid Dynamics 3 (7) (1991) 1760–1765.
[34] C. Meneveau, T. S. Lund, W. H. Cabot, A lagrangian dynamic subgrid-scale model of turbulence, Journal of fluid mechanics 319 (1996) 353–385.
[35] P. Huerre, P. A. Monkewitz, Local and global instabilities in spatially developing flows, Annual review of fluid mechanics 22 (1) (1990) 473–537.
[36] M. M. Rogers, R. D. Moser, The three-dimensional evolution of a plane mixing layer: the kelvin–helmholtz rollup, Journal of Fluid Mechanics 243 (1992) 183–226.
[37] R. D. Moser, M. M. Rogers, The three-dimensional evolution of a plane mixing layer: pairing and transition to turbulence, Journal of Fluid Mechanics 247 (1) (1993) 275.
[38] M. Slessor, C. Bond, P. Dimotakis, Turbulent shear-layer mixing at high reynolds numbers: effects of inflow conditions, Journal of Fluid Mechanics 376 (1998) 115–138.
[39] E. Balaras, U. Piomelli, J. M. Wallace, Self-similar states in turbulent mixing layers, Journal of Fluid Mechanics 446 (2001) 1–24.
[40] P. K. Sweby, High resolution schemes using flux limiters for hyperbolic conservation laws, SIAM journal on numerical analysis 21 (5) (1984) 995–1011.
[41] S. T. Zalesak, Fully multidimensional flux-corrected transport algorithms for fluids, Journal of computational physics 31 (3) (1979) 335–362.
[42] R. J. LeVeque, Numerical methods for conservation laws. 1992, BirkhaØ user Basel.
[43] N. A. Adams, K. Shariff, A high-resolution hybrid compact-eno scheme for shock-turbulence interaction problems, Journal of Computational Physics 127 (1) (1996) 27–51.
[44] S. Pirozzoli, Conservative hybrid compact-weno schemes for shock-turbulence interaction, Journal of Computational Physics 178 (1) (2002) 81–117.
[45] D. J. Hill, D. I. Pullin, Hybrid tuned center-difference-weno method for large eddy simulations in the presence of strong

shocks, Journal of Computational Physics 194 (2) (2004) 435–450.
[46] G. Ward, D. Pullin, A hybrid, center-difference, limiter method for simulations of compressible multicomponent flows with mie-grüneisen equation of state, Journal of Computational Physics 229 (8) (2010) 2999–3018.
[47] S. Osher, S. Chakravarthy, High resolution schemes and the entropy condition, SIAM Journal on Numerical Analysis 21 (5) (1984) 955–984.
[48] C.-W. Shu, S. Osher, Efficient implementation of essentially non-oscillatory shock-capturing schemes, Journal of Computational Physics 77 (2) (1988) 439–471.
[49] A. Harten, B. Engquist, S. Osher, S. R. Chakravarthy, Uniformly high order accurate essentially non-oscillatory schemes, iii, Journal of computational physics 71 (2) (1987) 231–303.
[50] M. Dumbser, O. Zanotti, A. Hidalgo, D. S. Balsara, Ader-weno finite volume schemes with space–time adaptive mesh refinement, Journal of Computational Physics 248 (2013) 257–286.
[51] X.-D. Liu, S. Osher, T. Chan, Weighted essentially non-oscillatory schemes, Journal of computational physics 115 (1) (1994) 200–212.
[52] G.-S. Jiang, C.-W. Shu, Efficient implementation of weighted eno schemes, Journal of computational physics 126 (1) (1996) 202–228.
[53] A. Arakawa, V. R. Lamb, Computational design of the basic dynamical processes of the ucla general circulation model, Methods in computational physics 17 (1977) 173–265.
[54] U. Schumann, Algorithms for direct numerical simulation of shear-periodic turbulence, in: Ninth International Conference on Numerical Methods in Fluid Dynamics, Springer, 1985, pp. 492–496.
[55] G. Matheou, D. Chung, L. Nuijens, B. Stevens, J. Teixeira, On the fidelity of large-eddy simulation of shallow precipitating cumulus convection, Monthly Weather Review 139 (9) (2011) 2918–2939.
[56] G. Matheou, D. Chung, Large-eddy simulation of stratified turbulence. part ii: Application of the stretched-vortex model to the atmospheric boundary layer, Journal of the Atmospheric Sciences 71 (12) (2014) 4439–4460.
[57] G. Matheou, K. W. Bowman, A recycling method for the large-eddy simulation of plumes in the atmospheric boundary layer, Environmental Fluid Mechanics 16 (1) (2016) 69–85.
[58] N. Sharan, Time-stable high-order finite difference methods for overset grids, Ph.D. thesis, University of Illinois at Urbana-Champaign (2016).
[59] N. Sharan, C. Pantano, D. J. Bodony, Time-stable overset grid method for hyperbolic problems using summation-by-parts operators, Journal of Computational Physics 361 (2018) 199–230.
[60] N. Sharan, C. Pantano, D. J. Bodony, Energy stable overset grid methods for hyperbolic problems, in: 7th AIAA Theoretical Fluid Mechanics Conference, 2014, p. 2924.
[61] R. Mittal, P. Moin, Suitability of upwind-biased finite difference schemes for large-eddy simulation of turbulent flows, AIAA Journal-American Institute of Aeronautics and Astronautics 35 (8) (1997) 1415–1416.
[62] S. Ghosal, Mathematical and physical constraints on large-eddy simulation of turbulence, AIAA journal 37 (4).
[63] B. P. Leonard, A stable and accurate convective modelling procedure based on quadratic upstream interpolation, Computer methods in applied mechanics and engineering 19 (1) (1979) 59–98.
[64] B. Van Leer, Towards the ultimate conservative difference scheme. iv. a new approach to numerical convection, Journal of computational physics 23 (3) (1977) 276–299.
[65] S. K. Lele, Compact finite difference schemes with spectral-like resolution, Journal of computational physics 103 (1) (1992) 16–42.
[66] S. Pirozzoli, On the spectral properties of shock-capturing schemes, Journal of Computational Physics 219 (2) (2006) 489–497.
[67] H. Pitsch, O. Desjardins, G. Balarac, M. Ihme, Large-eddy simulation of turbulent reacting flows, Progress in Aerospace Sciences 44 (6) (2008) 466–478.
[68] S. L. Graham, P. B. Kessler, M. K. Mckusick, Gprof: A call graph execution profiler, in: ACM Sigplan Notices, Vol. 17, ACM, 1982, pp. 120–126.
[69] M. P. Martín, E. M. Taylor, M. Wu, V. G. Weirs, A bandwidth-optimized weno scheme for the effective direct numerical simulation of compressible turbulence, Journal of Computational Physics 220 (1) (2006) 270–289.
[70] A. K. Henrick, T. D. Aslam, J. M. Powers, Mapped weighted essentially non-oscillatory schemes: achieving optimal order near critical points, Journal of Computational Physics 207 (2) (2005) 542–567.
[71] R. Borges, M. Carmona, B. Costa, W. S. Don, An improved weighted essentially non-oscillatory scheme for hyperbolic conservation laws, Journal of Computational Physics 227 (6) (2008) 3191–3211.
[72] X. Hu, Q. Wang, N. A. Adams, An adaptive central-upwind weighted essentially non-oscillatory scheme, Journal of Computational Physics 229 (23) (2010) 8952–8965.
[73] P. E. Dimotakis, Turbulent free shear layer mixing and combustion, Communications in Computational Physics 137 (Eds., S.N.B. Murthy and E.T. Curan, AIAA, Washington, DC) (1991) Ch. 5, 265–340.